

Experimental Demonstration of a Decentralized Electromagnetic Formation Flying Control Using Alternating Magnetic Field Forces

Sumit S. Kamat, Ajin Sunny, T. Michael Seigler, and Jesse B. Hoagg*

Department of Mechanical and Aerospace Engineering, University of Kentucky, Lexington, KY 40506-0503

Abstract

Electromagnetic formation flying (EMFF) is challenging due to the complex coupling between the electromagnetic fields generated by each satellite in the formation. To address this challenge, this article uses alternating magnetic field forces (AMFF) to decouple the electromagnetic forces between each pair of satellites. The key idea of AMFF is that a pair of alternating (e.g., sinusoidal) magnetic moments results in a nonzero time-averaged interaction force if and only if those alternating magnetic moments have the same frequency. Hence, the approach in this article is to drive each satellite's electromagnetic actuation system with a sum of sinusoids, where each frequency is common to only a pair of satellites. Then, the amplitudes of each sinusoid are modulated (i.e., controlled) to achieve the desired forces between each pair of satellites. The main contribution of this article is a 3-satellite experimental demonstration of decentralized closed-loop EMFF using AMFF. To the authors' knowledge, this is the first demonstration of AMFF with at least 3 satellites in open or closed loop. This is noteworthy because the coupling challenges of EMFF are only present with more than 2 satellites, and thus, a formation of at least 3 is necessary to evaluate the effectiveness of AMFF. The experiments are conducted on a ground-based testbed consisting of 3 electromagnetically actuated satellites on linear air tracks. The closed-loop experiments demonstrate decentralized EMFF with AMFF where the mean steady-state formation error is less than 0.005 m, the maximum steady-state formation error is less than ± 0.01 m, and the settling time is less than 30 s. The closed-loop experimental results are compared with behavior from numerical simulations.

1. Notation

Physical vectors are denoted with bold symbols, for example, \mathbf{r} . The magnitude of \mathbf{r} is denoted by $|\mathbf{r}|$. A frame is a collection of mutually-orthogonal physical unit vectors.

Let \mathbb{N} denote the set of nonnegative integers. Let $\mathcal{I} \triangleq \{1, \dots, n\}$, where $n \in \mathbb{N}$ is the number of satellites in the formation, and $\mathcal{P} \triangleq \{(i, j) \in \mathcal{I} \times \mathcal{I} : i \neq j\}$, which is the set of ordered pairs. Unless otherwise stated, all statements in this paper that involve the subscript i , ij , and k are for all $i \in \mathcal{I}$, all $(i, j) \in \mathcal{P}$, and all $k \in \mathbb{N}$.

2. Nomenclature

$\mathcal{F} = [\mathbf{i} \quad \mathbf{j} \quad \mathbf{j}]$	Inertial frame
\mathbf{r}_i	Position of satellite i (m)
\mathbf{v}_i	Velocity of satellite i (m/s)
$\mathbf{r}_{ij} \triangleq \mathbf{r}_i - \mathbf{r}_j$	Relative position (m)
\mathbf{F}_{ij}	Force applied to satellite i by j (N)
\mathbf{f}	Intersatellite force function ($\text{A}^2\text{-m}^4$)
μ_0	Vacuum permeability constant (H/m)
m	Mass of each satellite (kg)
\mathbf{u}_i	Magnetic moment of satellite i ($\text{A}\text{-m}^2$)
\mathbf{d}_{ij}	Desired relative position (m)

ω_{ij}	Interaction frequency (rad/s)
$\mathbf{P}_{ij,k}$	Amplitude control ($\text{A}\text{-m}^2$)
T	Update period for control (s)
$\bar{\mathbf{F}}_{ij}$	Time-averaged intersatellite force (N)
$\hat{\mathbf{F}}_{ij}$	Approximate time-averaged intersatellite force (N)
$\mathbf{r}_{ij,k}$	Sampled relative position
$\mathbf{v}_{ij,k}$	Sampled relative velocity (m/s)
$\mathbf{f}_{ij,k}^*$	Desired value of $\mathbf{f}(\mathbf{r}_{ij,k}, \mathbf{p}_{ij,k}, \mathbf{p}_{ji,k})$ ($\text{A}^2\text{-m}^4$)
$\alpha_{ij}, \rho_{ij}, \beta$	Control gains
$r_{ij,k}$	Relative position in \mathbf{i} direction (m)
$v_{ij,k}$	Relative velocity in \mathbf{i} direction (m/s)
d_{ij}	Desired relative position in \mathbf{i} direction (m)
$f_{ij,k}^*$	$\mathbf{f}_{ij,k}^*$ in \mathbf{i} direction ($\text{A}^2\text{-m}^4$)
$p_{ij,k}$	Amplitude control in \mathbf{i} direction ($\text{A}\text{-m}^2$)
I_i	Current in the coil of satellite i (A)
$I_{ij,k}$	Current amplitude (A)
f	\mathbf{f} in \mathbf{i} direction ($\text{A}^2\text{-m}^4$)
$\xi_{ij,k}$	Integrator state (m)
I	Maximum allowable current (A)
$\hat{F}(r_{ij}, p_{ij}, p_{ji})$	$\hat{\mathbf{F}}_{ij}$ in \mathbf{i} direction (N)
$q_{ij,k}$	Measurement of r_{ij} (m)
$\hat{r}_{ij,k}$	Estimate of r_{ij} (m)
$\hat{v}_{ij,k}$	Estimate of v_{ij} (m/s)
V	Variance of noise associate with $q_{ij,k}$ (m^2)
L	Kalman filter gain

*Corresponding author; email: jesse.hoagg@uky.edu

P	Solution to algebraic Riccati equation
w	Variance of disturbance force (m^2/s^4)
\hat{r}_{os}	Overshoot (m)
T_s	Settling time (s)
$P_{\hat{F}}$	Root mean square of \hat{F} (N)

3. Introduction

Electromagnetic formation flying (EMFF) is accomplished using electromagnetic coils that are onboard satellites in a formation. Each satellite’s coils generate a magnetic field, which interacts with the magnetic fields of the other satellites to create magnetic field forces. These magnetic field forces can control the relative positions of satellites [1, 2, 3]. An advantage of EMFF is that the power source is renewable, while conventional actuation systems such as propellant thrusters eventually deplete.

EMFF for a single pair of satellites where the coils are driven by direct current (DC) is addressed in [4, 5]. Experiments using DC-driven coils are presented in [5]; this includes open-loop experiments as well as position-hold and trajectory-following experiments. In addition, feasibility experiments onboard the International Space Station are presented in [3], where attractive and repulsive forces were generated between 2 DC-driven coils.

EMFF for more than 2 satellites is challenging because the intersatellite forces are nonlinear functions of the magnetic moments generated by all satellites as well as the relative positions of all satellites. In other words, there is complex coupling between the electromagnetic fields generated by all satellites, and this coupling ultimately leads to intersatellite forces between every pair of satellites. EMFF control for more than 2 satellites is considered in [6, 7, 8]. However, these approaches require centralization of all measurement information and solving nonconvex constrained optimization problems that do not scale well to a large number of satellites. An alternative approach in [9] relies on scheduling the actuation of each EMFF satellite over time. In this case, only a subset of the satellites are actuated for each time interval, which limits computational complexity because control computations are computed for only a subset of satellites. However, this approach requires centralization of the schedule and the control is computed through a nonconvex optimization. In sum, the coupling between electromagnetic fields causes scalability and decentralization challenges for EMFF.

A different approach to EMFF is to use alternating magnetic field forces (AMFF) to address the challenge of coupling between the electromagnetic fields. The key idea of AMFF is that a pair of alternating (e.g., sinusoidal) magnetic moments results in a nonzero average interaction force between a pair of satellites if and only if those alternating magnetic moments have the same frequency [10, 11].

A decentralized EMFF method using AMFF is presented in [12]. In this method, each satellite computes its desired intersatellite forces using measurements of its

position and velocity relative to only its local neighbor satellites, avoiding the centralization and scalability limitations discussed above. Then, each satellite uses a sum of frequency-multiplexed sinusoidal magnetic moments to achieve desired intersatellite forces between each pair of satellites. For example, consider 3 satellites, where satellite 1 generates a magnetic moment that is the sum of sinusoids at 10 Hz and 20 Hz, satellite 2 generates a magnetic moment at 10 Hz, and satellite 3 generates a magnetic moment at 20 Hz. In this scenario, the average force between satellites 1 and 2 is a function of the amplitudes of the sinusoids at the common frequency 10 Hz. Notably, the average force between satellites 1 and 2 is independent of the sinusoidal amplitudes at 20 Hz. Similarly, the average force between satellites 1 and 3 is a function of the amplitudes at the common frequency 20 Hz. Finally, since the magnetic moments of satellites 2 and 3 do not have a common frequency, the average force between these satellites is negligible.

In addition to [12], EMFF using AMFF has been explored in [13, 14, 15, 16, 17, 18]. For example, [13, 14] presents a leader-following method with AMFF using sliding-mode control. Relative position and attitude control with AMFF is addressed with a centralized algorithm in [18] and using a decentralized algorithm in [15]. In [16, 17], AMFF is combined with traditional reaction wheels in a centralized algorithm for relative position and attitude control in the presence of disturbance torques caused by interaction with Earth’s magnetic field.

Experimental evaluations of EMFF with AMFF are in [11, 19, 20]. Open-loop experiments demonstrating the AMFF approach are presented in [11]. Closed-loop single-degree-of-freedom experiments with a pair of satellites on linear air-tracks are presented in [19, 20]. Note that since AMFF uses sinusoidal currents, it can be implemented with standard coils (as demonstrated in [11, 19, 20]) as opposed to superconducting coils, which have been used in DC-actuation experiments. Since the coupling challenges of EMFF are only present with more than 2 satellites, a formation of at least 3 satellites is necessary to evaluate the effectiveness of AMFF. However, to the authors’ knowledge, the existing literature does not include any experiments using AMFF with more than 2 satellites

The main contribution of this article is an experimental demonstration of closed-loop EMFF using AMFF with 3 satellites. This is the first demonstration of AMFF with at least 3 satellites in open or closed loop. This work demonstrates EMFF with 3 satellites on a linear air track, where the coil of the center satellite is driven by a sum of 2 AC currents and each outer satellite is driven by one of the AC currents. As a result, intersatellite forces are generated between the center satellite and each outer satellite. This article adopts the piecewise-sinusoidal magnetic moment approach in [12] to address the challenges of coupling between the electromagnetic fields; this approach is reviewed in Section 6. Then, Section 7 presents the closed-loop decentralized EMFF algorithm, which is adopted from [12]

but with a simplified approach for the control amplitude allocation. Section 8 describes the experimental testbed and modifies the EMFF control to account for hardware limitations such as sensor noise and amplitude saturation in the control current. Experimental results are presented in Section 9. First, this article presents open- and closed-loop experiments with 2 satellites to demonstrate the feasibility of EMFF with AMFF. Next, this article presents closed-loop experiments with 3 satellites, where the satellites achieve formation in less than 30 s with mean steady-state error less than 0.005 m and maximum steady-state formation error is less than ± 0.01 m. This experiment demonstrates the decoupling principle of frequency-multiplexed AMFF.

4. Method Overview

The core concept of AMFF is that a pair of sinusoidal magnetic moments results in a nonzero time-averaged interaction force between a pair of satellites if and only if those alternating magnetic moments have the same frequency. The method in this paper is decentralized, which means that each satellite has access to measurements of its position and velocity relative to only its local neighbor satellites. First, this article presents a time-averaged model for the dynamics of a satellite formation, where the controllable magnetic moments are a sum of amplitude-modulated sinusoids. Next, the article shows how the sinusoidal amplitudes are selected to achieve desired intersatellite forces, which are determined decentrally by each satellite using feedback of its neighbors.

The main contribution of this article is the first experimental demonstration of EMFF using AMFF with more than 2 satellites. First, open- and closed-loop experiments are conducted with 2 satellites to demonstrate feasibility of AMFF. Next, closed loop experiments with 3 satellites are performed to demonstrate the core concept of AMFF.

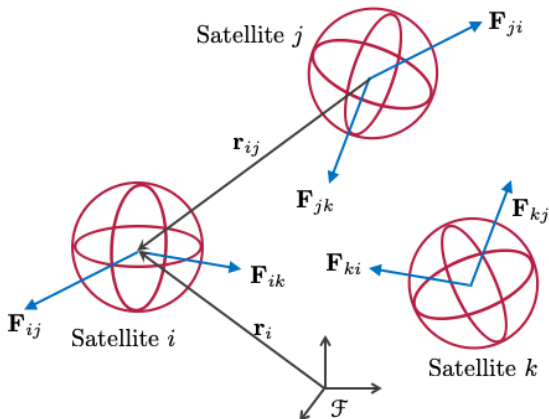


Figure 1: Each satellite is equipped with an electromagnetic actuation system consisting of three orthogonal coils. The relative positions of the satellites are controlled by the interaction of equal-and-opposite intersatellite forces produced by the actuation systems.

5. Satellite Dynamics

Consider a system of n satellites, where each satellite has mass m . The position \mathbf{r}_i locates the mass center of satellite i relative to the origin of an inertial frame \mathcal{F} which consists of the right-handed set of mutually orthogonal unit vectors $[\mathbf{i} \ \mathbf{j} \ \mathbf{k}]$. The velocity \mathbf{v}_i and acceleration $\dot{\mathbf{v}}_i$ are the first and the second time-derivatives of \mathbf{r}_i with respect to \mathcal{F} . The relative position $\mathbf{r}_{ij} \triangleq \mathbf{r}_i - \mathbf{r}_j$ locates the mass center of satellite i relative to the mass center of satellite j . The relative velocity \mathbf{v}_{ij} is the time derivative of \mathbf{r}_{ij} with respect to \mathcal{F} . The satellite system is shown in Figure 1.

Each satellite has an electromagnetic actuation system (i.e., multiple electromagnetic coils) that creates a magnetic field. These magnetic fields interact to produce intersatellite forces, which control the satellites' relative positions. The coils are modeled as magnetic dipoles, and the resulting force applied to satellite i by satellite j is

$$\mathbf{F}_{ij} = \frac{3\mu_0}{4\pi|\mathbf{r}_{ij}|^4} \mathbf{f}(\mathbf{r}_{ij}, \mathbf{u}_i, \mathbf{u}_j), \quad (1)$$

where μ_0 is the vacuum permeability constant, \mathbf{u}_i is the magnetic moment of satellite i , and the intersatellite force function is

$$\begin{aligned} \mathbf{f}(\mathbf{r}_{ij}, \mathbf{u}_i, \mathbf{u}_j) \triangleq & \left(\mathbf{u}_j \cdot \frac{\mathbf{r}_{ij}}{|\mathbf{r}_{ij}|} \right) \mathbf{u}_i + \left(\mathbf{u}_i \cdot \frac{\mathbf{r}_{ij}}{|\mathbf{r}_{ij}|} \right) \mathbf{u}_j \\ & + \left[(\mathbf{u}_i \cdot \mathbf{u}_j) - 5 \left(\mathbf{u}_i \cdot \frac{\mathbf{r}_{ij}}{|\mathbf{r}_{ij}|} \right) \left(\mathbf{u}_j \cdot \frac{\mathbf{r}_{ij}}{|\mathbf{r}_{ij}|} \right) \right] \frac{\mathbf{r}_{ij}}{|\mathbf{r}_{ij}|}. \end{aligned} \quad (2)$$

The magnetic moment \mathbf{u}_i , which is the control of satellite i , is a function of the current supplied to the electromagnetic coils. Since $\mathbf{r}_{ij} = -\mathbf{r}_{ji}$, it follows from (1) and (2) that $\mathbf{F}_{ij} = -\mathbf{F}_{ji}$, that is, the force applied to satellite j by i is equal and opposite the force applied to i by j . See [6] and [7] for more information on (1) and (2).

The translational dynamics of satellite i are

$$\dot{\mathbf{v}}_i \triangleq \frac{c_0}{m} \sum_{j \in \mathcal{I} \setminus \{i\}} \frac{1}{|\mathbf{r}_{ij}|^4} \mathbf{f}(\mathbf{r}_{ij}, \mathbf{u}_i, \mathbf{u}_j), \quad (3)$$

where $c_0 \triangleq 3\mu_0/(4\pi)$. Since $\mathbf{F}_{ij} = -\mathbf{F}_{ji}$, it follows from (3) that $\sum_{i \in \mathcal{I}} \dot{\mathbf{v}}_i(t) = 0$, which implies that the linear momentum of the system of satellites is conserved. Thus, the intersatellite electromagnetic forces can be used to alter relative positions, but they have no effect on the overall mass center of the satellites. Therefore, traditional actuation systems may be needed in combination with EMFF to control the formation's mass center. For example, propellant thrusters may be needed for orbit maintenance in the presence of disturbances (e.g., atmospheric drag in low Earth orbit) or to allow for orbit transfers. Similarly, a traditional attitude control system, such as reaction wheels, could be required for attitude control and addressing disturbances such as torques introduced by interactions with the Earth's magnetic field.

Let the constant \mathbf{d}_{ij} be the desired position of satellite i relative to satellite j , where $\mathbf{d}_{ij} = -\mathbf{d}_{ji}$. The objective is to design and demonstrate a decentralized control method that relies on feedback of neighboring satellites and yields $\lim_{t \rightarrow \infty} \mathbf{r}_{ij}(t) = \mathbf{d}_{ij}$.

6. Time-Averaged Formation Dynamics with Sinusoidal Controls

This section reviews the piecewise-sinusoidal magnetic-moment approach in [12], which is used to address the coupling that occurs between electromagnetic fields. This approach enables decentralized formation control, where each satellite uses relative position and velocity measurements of only its neighbors. In this approach, each satellite uses a piecewise-sinusoidal magnetic moment \mathbf{u}_i that is the sum of up to $n - 1$ sinusoids with unique frequencies. Each unique frequency is common to only one pair of satellites. Thus, there are a total of up to $n(n - 1)/2$ unique frequencies, and the amplitudes of each common-frequency pair of sinusoids are selected to prescribe the time-averaged intersatellite force between the associated satellite pair.

Let $\omega_{ij} \geq 0$ be the interaction frequency between satellite i and j , where $\omega_{ij} = \omega_{ji}$ is unique if it is nonzero. If an interaction frequency is zero, then the time-averaged intersatellite force between the associated satellite pair is zero. Next, let $T > 0$ be a common multiple of $\{2\pi/\omega_{ij} : (i, j) \in \mathcal{P} \text{ and } \omega_{ij} \neq 0\}$. For all $k \in \mathbb{N}$ and $t \in [kT, kT + T)$, consider the piecewise-sinusoidal control

$$\mathbf{u}_i(t) = \sum_{j \in \mathcal{I} \setminus \{i\}} \mathbf{p}_{ij,k} \sin \omega_{ij} t \quad (4)$$

where the amplitudes $\{\mathbf{p}_{ij,k}\}_{k=0}^{\infty}$ are the control variables.

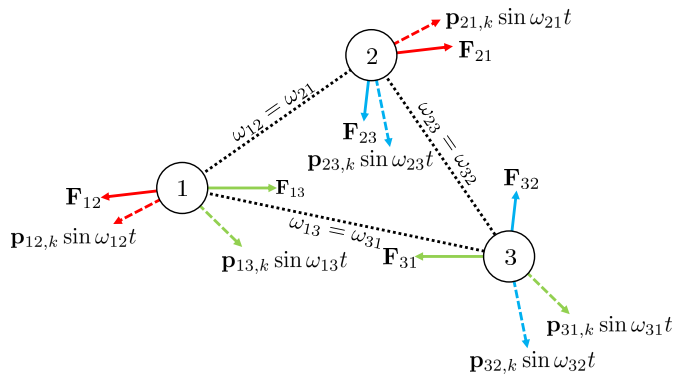


Figure 2: AMFF with 3 satellites and unique frequencies $\omega_{12} = \omega_{21}$, $\omega_{13} = \omega_{31}$, and $\omega_{23} = \omega_{32}$. For each pair of satellites, the intersatellite forces $\mathbf{F}_{ij} = -\mathbf{F}_{ji}$ are determined on average from the amplitudes $(\mathbf{p}_{ij,k}, \mathbf{p}_{ji,k})$ at frequency ω_{ij} .

The key idea of AMFF is that the amplitude pair $(\mathbf{p}_{ij,k}, \mathbf{p}_{ji,k})$ at the common frequency ω_{ij} determines the time-averaged forces between satellites i and j . Figure 2 illustrates this concept for 3 satellites, where the components of \mathbf{u}_i and \mathbf{u}_j at ω_{ij} cause the time-averaged forces between satellites i and j . The following result characterizes this

decoupling property, which allows us to formalize the core concept of AMFF. The result is from [12, Proposition 1], and it is a consequence of averaging the product of sinusoids over an integer number of periods.

Proposition 1. Let $i, j \in \mathbb{N}$, and let \mathbf{r} be a constant. Then, for all $k \in \mathbb{N}$,

$$\frac{1}{T} \int_{kT}^{kT+T} \mathbf{f}(\mathbf{r}, \mathbf{u}_i(t), \mathbf{u}_j(t)) dt \triangleq \frac{1}{2} \mathbf{f}(\mathbf{r}, \mathbf{p}_{ij,k}, \mathbf{p}_{ji,k}).$$

We use Proposition 1 to derive a time-averaged model of the dynamics (3). Integrating (3) over the interval $[kT, kT + T]$ yields

$$\mathbf{v}_i(kT + T) = \mathbf{v}_i(kT) + \frac{T}{m} \sum_{j \in \mathcal{I} \setminus \{i\}} \bar{\mathbf{F}}_{ij}(k), \quad (5)$$

where the time-averaged intersatellite force is

$$\bar{\mathbf{F}}_{ij}(k) \triangleq \frac{1}{T} \int_{kT}^{kT+T} \frac{c_0}{|\mathbf{r}_{ij}(t)|^4} \mathbf{f}(\mathbf{r}_{ij}(t), \mathbf{u}_i(t), \mathbf{u}_j(t)) dt.$$

We define the *approximate time-averaged intersatellite force*

$$\hat{\mathbf{F}}_{ij,k} \triangleq \frac{1}{T} \int_{kT}^{kT+T} \frac{c_0}{|\mathbf{r}_{ij,k}|^4} \mathbf{f}(\mathbf{r}_{ij,k}, \mathbf{u}_i(t), \mathbf{u}_j(t)) dt, \quad (6)$$

which is an approximation of $\bar{\mathbf{F}}_{ij,k}$ obtained by replacing $\mathbf{r}_{ij}(t)$ with its sampling $\mathbf{r}_{ij,k} \triangleq \mathbf{r}_{ij}(kT)$. Proposition 1 implies that

$$\hat{\mathbf{F}}_{ij,k} = \frac{c_0}{2|\mathbf{r}_{ij,k}|^4} \mathbf{f}(\mathbf{r}_{ij,k}, \mathbf{p}_{ij,k}, \mathbf{p}_{ji,k}). \quad (7)$$

Note that $(\hat{\mathbf{F}}_{ij,k}, \hat{\mathbf{F}}_{ji,k})$ depends on the amplitude control pair $(\mathbf{p}_{ij,k}, \mathbf{p}_{ji,k})$, which does not affect the approximate time-averaged intersatellite force between any other pair of satellites. Thus, if \mathbf{r}_{ij} does not change significantly over $[kT, kT + T)$, then the time-averaged formation dynamics can be approximated by (5) with $\bar{\mathbf{F}}_{ij}(k)$ replaced by $\hat{\mathbf{F}}_{ij,k}$.

7. EMFF Control Algorithm

7.1. Desired Intersatellite Forces

The intersatellite feedback structure is described using an undirected graph. The vertex set of the undirected graph is \mathcal{I} . Let $\mathcal{E} \subset \mathcal{I} \times \mathcal{I}$ be the edge set. We assume that the undirected graph $\mathcal{G} = (\mathcal{I}, \mathcal{E})$ is connected. The neighbor set of satellite i is $\mathcal{N}_i \triangleq \{j \in \mathcal{I} : (i, j) \in \mathcal{E}\}$, and satellite i has access to $\{\mathbf{r}_{ij,k}\}_{j \in \mathcal{N}_i}$ and $\{\mathbf{v}_{ij,k}\}_{j \in \mathcal{N}_i}$ for feedback, where $\mathbf{v}_{ij,k} \triangleq \mathbf{v}_i(kT) - \mathbf{v}_j(kT)$.

Define the desired value for the intersatellite force function

$$\mathbf{f}_{ij,k}^* \triangleq -\frac{2m|\mathbf{r}_{ij,k}|^4}{c_0} \alpha_{ij}((\mathbf{r}_{ij,k} - \mathbf{d}_{ij}) + \beta \mathbf{v}_{ij,k}) \quad (8)$$

where $\alpha_{ij} = \alpha_{ji} \geq 0$ and $\beta > 0$ are feedback gains. If $(i, j) \notin \mathcal{E}$, then $\alpha_{ij} = 0$; otherwise, $\alpha_{ij} > 0$.

If $\mathbf{f}(\mathbf{r}_{ij,k}, \mathbf{p}_{ij,k}, \mathbf{p}_{ji,k}) = \mathbf{f}_{ij,k}^*$, then it follows from (7) that

$$\hat{\mathbf{F}}_{ij,k} = -m\alpha_{ij}[(\mathbf{r}_{ij,k} - \mathbf{d}_{ij}) + \beta\mathbf{v}_{ij,k}]. \quad (9)$$

In this case, [12, Theorem 5] provides conditions on selecting the gains α_{ij} and β such that the formation error $\mathbf{r}_{ij,k} - \mathbf{d}_{ij}$ tends to zero for $\bar{\mathbf{F}}_{ij}(k) = \hat{\mathbf{F}}_{ij,k}$. The approximate time-averaged intersatellite force (9) is based on linear consensus for sampled-data double integrators [21]. This method uses feedback to determine approximate time-averaged intersatellite forces $\hat{\mathbf{F}}_{ij,k}$ that create virtual linear springs and dashpots between satellite i and j . We note that larger α_{ij} tends to result in faster formation convergence but can cause oscillations (e.g., overshoot) in the response. Larger β increases the virtual intersatellite damping and tends to reduce oscillations. We also note that the analysis in [12, Theorem 5] relies on the assumption that $\bar{\mathbf{F}}_{ij}(k) = \hat{\mathbf{F}}_{ij,k}$, which is a reasonable approximation if \mathbf{r}_{ij} does not change significantly over $[kT, kT + T)$.

7.2. Control Amplitude Pair To Achieve Prescribed Intersatellite Force

This section provides a construction for the amplitude pair $(\mathbf{p}_{ij,k}, \mathbf{p}_{ji,k})$ such that $\mathbf{f}(\mathbf{r}_{ij,k}, \mathbf{p}_{ij,k}, \mathbf{p}_{ji,k}) = \mathbf{f}_{ij,k}^*$. This amplitude pair is constructed from $\mathbf{r}_{ij,k}$ and $\mathbf{f}_{ij,k}^*$. The construction is presented in [22, 23] for physical vectors resolved in an inertial frame. Here, we present the construction coordinate free. The following functions of a relative position \mathbf{r} and desired force function value \mathbf{f}^* are needed to construct the control amplitudes. Specifically, we define

$$\mathbf{g}(\mathbf{r}, \mathbf{f}^*) \triangleq \begin{cases} \frac{g_r(\mathbf{r}, \mathbf{f}^*)}{|\mathbf{r}|} \mathbf{r} + \frac{g_{\text{rf}}(\mathbf{r}, \mathbf{f}^*)}{|\mathbf{r}||\mathbf{r} \times \mathbf{f}^*|} ((\mathbf{r} \times \mathbf{f}^*) \times \mathbf{r}), & \mathbf{r} \times \mathbf{f}^* \neq \mathbf{0}, \\ \frac{g_r(\mathbf{r}, \mathbf{f}^*)}{|\mathbf{r}|} \mathbf{r}, & \mathbf{r} \times \mathbf{f}^* = \mathbf{0}, \end{cases} \quad (10)$$

$$\mathbf{h}(\mathbf{r}, \mathbf{f}^*) \triangleq \begin{cases} \frac{h_r(\mathbf{r}, \mathbf{f}^*)}{|\mathbf{r}|} \mathbf{r} + \frac{h_{\text{rf}}(\mathbf{r}, \mathbf{f}^*)}{|\mathbf{r}||\mathbf{r} \times \mathbf{f}^*|} ((\mathbf{r} \times \mathbf{f}^*) \times \mathbf{r}), & \mathbf{r} \times \mathbf{f}^* \neq \mathbf{0}, \\ \frac{h_r(\mathbf{r}, \mathbf{f}^*)}{|\mathbf{r}|} \mathbf{r}, & \mathbf{r} \times \mathbf{f}^* = \mathbf{0}, \end{cases} \quad (11)$$

where

$$g_r(\mathbf{r}, \mathbf{f}^*) \triangleq -\frac{\text{sgn}(\mathbf{r} \cdot \mathbf{f}^*)}{2} \left(\frac{|\mathbf{r} \cdot \mathbf{f}^*| + \Phi_1(\mathbf{r}, \mathbf{f}^*)}{|\mathbf{r}|} \right)^{\frac{1}{2}}, \quad (12)$$

$$g_{\text{rf}}(\mathbf{r}, \mathbf{f}^*) \triangleq \frac{1}{\sqrt{2}} \left(\frac{-|\mathbf{r} \cdot \mathbf{f}^*| + \Phi_2(\mathbf{r}, \mathbf{f}^*)}{|\mathbf{r}|} \right)^{\frac{1}{2}}, \quad (13)$$

$$h_r(\mathbf{r}, \mathbf{f}^*) \triangleq \frac{1}{2} \left(\frac{|\mathbf{r} \cdot \mathbf{f}^*| + \Phi_2(\mathbf{r}, \mathbf{f}^*)}{|\mathbf{r}|} \right)^{\frac{1}{2}}, \quad (14)$$

$$h_{\text{rf}}(\mathbf{r}, \mathbf{f}^*) \triangleq -\frac{\text{sgn}(\mathbf{r} \cdot \mathbf{f}^*)}{\sqrt{2}} \left(\frac{-|\mathbf{r} \cdot \mathbf{f}^*| + \Phi_1(\mathbf{r}, \mathbf{f}^*)}{|\mathbf{r}|} \right)^{\frac{1}{2}}, \quad (15)$$

and

$$\Phi_1(\mathbf{r}, \mathbf{f}^*) \triangleq \sqrt{|\mathbf{r} \times \mathbf{f}^*|^2 + |\mathbf{r}|^2 |\mathbf{f}^*|^2}, \quad (16)$$

$$\Phi_2(\mathbf{r}, \mathbf{f}^*) \triangleq (2 - \text{sgn}(\mathbf{r} \cdot \mathbf{f}^*)) \Phi_1(\mathbf{r}, \mathbf{f}^*). \quad (17)$$

The following result shows that (10) and (11) are an amplitude pair such that \mathbf{f} takes on the prescribed value \mathbf{f}^* .

Proposition 2. For all \mathbf{f}^* and all $\mathbf{r} \neq \mathbf{0}$,

$$\mathbf{f}(\mathbf{r}, \mathbf{g}(\mathbf{r}, \mathbf{f}^*), \mathbf{h}(\mathbf{r}, \mathbf{f}^*)) = \mathbf{f}^*.$$

Proposition 2 shows how to select the amplitudes $\mathbf{p}_{ij,k}$ and $\mathbf{p}_{ji,k}$ of the common frequency sinusoids in (4). In other words, Proposition 2 implies that we can use (10) and (11) to select $(\mathbf{p}_{ij,k}, \mathbf{p}_{ji,k})$ such that $\mathbf{f}(\mathbf{r}_{ij,k}, \mathbf{p}_{ij,k}, \mathbf{p}_{ji,k}) = \mathbf{f}_{ij,k}^*$, which implies that the approximate time-averaged intersatellite force equals the desired value given by (9). Specifically, we let the amplitudes be

$$\mathbf{p}_{ij,k} = \begin{cases} \mathbf{g}(\mathbf{r}_{ij,k}, \mathbf{f}_{ij,k}^*), & i < j, \\ \mathbf{h}(\mathbf{r}_{ij,k}, \mathbf{f}_{ij,k}^*), & i > j. \end{cases} \quad (18)$$

It follows from Proposition 2 that $\mathbf{f}(\mathbf{r}_{ij,k}, \mathbf{p}_{ij,k}, \mathbf{p}_{ji,k}) = \mathbf{f}_{ij,k}^*$. In other words, the amplitude pair $(\mathbf{p}_{ij,k}, \mathbf{p}_{ji,k})$ given by (18) achieves the desired value of the intersatellite force function (8).

Proof of Proposition 2. We consider 2 cases: (i) $\mathbf{r} \times \mathbf{f}^* \neq \mathbf{0}$ and (ii) $\mathbf{r} \times \mathbf{f}^* = \mathbf{0}$.

First, consider (i) $\mathbf{r} \times \mathbf{f}^* \neq \mathbf{0}$. Substituting $|\mathbf{r} \times \mathbf{f}^*| = |\mathbf{r}|^2 \mathbf{f}_* - (\mathbf{r} \cdot \mathbf{f}_*) \mathbf{r}$, (10), and (11) into (2) yields

$$\mathbf{f}(\mathbf{r}, \mathbf{g}, \mathbf{h}) = \left(-\frac{2g_r h_r}{|\mathbf{r}|} + \frac{g_{\text{rf}} h_{\text{rf}}}{|\mathbf{r}|} - \frac{(g_r h_{\text{rf}} + g_{\text{rf}} h_r)(\mathbf{r} \cdot \mathbf{f}_*)}{|\mathbf{r}||\mathbf{r} \times \mathbf{f}_*|} \right) \mathbf{r} + \frac{(g_r h_{\text{rf}} + g_{\text{rf}} h_r) |\mathbf{r}|}{|\mathbf{r} \times \mathbf{f}_*|} \mathbf{f}_*. \quad (19)$$

where the arguments \mathbf{r} and \mathbf{f}_* are omitted for brevity. We consider 2 subcases: $\mathbf{r} \cdot \mathbf{f}_* = 0$ and $\mathbf{r} \cdot \mathbf{f}_* \neq 0$. For $\mathbf{r} \cdot \mathbf{f}_* = 0$, it follows from (12)–(15) that $g_r = h_{\text{rf}} = 0$ and $g_{\text{rf}} h_r = |\mathbf{r} \times \mathbf{f}_*|/|\mathbf{r}|$, and substituting into (19) yields $\mathbf{f}(\mathbf{r}, \mathbf{g}, \mathbf{h}) = \mathbf{f}_*$. Next, for $\mathbf{r} \cdot \mathbf{f}_* \neq 0$, it follows from (16) and (17) that $\Phi_2 = \Phi_1$, and using (12)–(15) yields

$$g_r h_r = -\frac{\text{sgn}(\mathbf{r} \cdot \mathbf{f}_*)}{4|\mathbf{r}|} (|\mathbf{r} \cdot \mathbf{f}_*| + \Phi_1),$$

$$g_r h_{\text{rf}} = g_{\text{rf}} h_r = \frac{|\mathbf{r} \times \mathbf{f}_*|}{2|\mathbf{r}|},$$

$$a_y b_y = -\frac{\text{sgn}(\mathbf{r} \cdot \mathbf{f}_*)}{2|\mathbf{r}|} (-|\mathbf{r} \cdot \mathbf{f}_*| + \Phi_1).$$

Thus, substituting into (19) yields $\mathbf{f}(\mathbf{r}, \mathbf{g}, \mathbf{h}) = \mathbf{f}_*$, which confirms the result for (i) $\mathbf{r} \times \mathbf{f}^* \neq \mathbf{0}$.

Next, consider (ii) $\mathbf{r} \times \mathbf{f}^* = \mathbf{0}$, and substituting (10)–(15) into (2) yields

$$\begin{aligned} \mathbf{f}(\mathbf{r}, \mathbf{g}, \mathbf{h}) &= -2g_r h_r \frac{\mathbf{r}}{|\mathbf{r}|} \\ &= \frac{\text{sgn}(\mathbf{r} \cdot \mathbf{f}_*)}{2|\mathbf{r}|^2} (|\mathbf{r} \cdot \mathbf{f}_*| + \Phi_1)^{\frac{1}{2}} (|\mathbf{r} \cdot \mathbf{f}_*| + \Phi_2)^{\frac{1}{2}} \mathbf{r}. \end{aligned} \quad (20)$$

We consider 2 subcases: $\mathbf{r} \cdot \mathbf{f}_* = 0$ and $\mathbf{r} \cdot \mathbf{f}_* \neq 0$. For $\mathbf{r} \cdot \mathbf{f}_* = 0$, it follows from (20) that $\mathbf{f}(\mathbf{r}, \mathbf{g}, \mathbf{h}) = \mathbf{0}$. Since $\mathbf{r} \cdot \mathbf{f}_* = 0$ and $\mathbf{r} \times \mathbf{f}_* = \mathbf{0}$, it follows that $\mathbf{f}_* = \mathbf{0}$, which implies that $\mathbf{f}(\mathbf{r}, \mathbf{g}, \mathbf{h}) = \mathbf{f}_*$. Next, for $\mathbf{r} \cdot \mathbf{f}_* \neq 0$, it follows from (16) and (17) that $\Phi_2 = \Phi_1$. Since $\mathbf{r} \cdot \mathbf{f}_* \neq 0$ and $\mathbf{r} \times \mathbf{f}_* = \mathbf{0}$, it follows that $\mathbf{r} = (\text{sgn}(\mathbf{r} \cdot \mathbf{f}_*)|\mathbf{r}|/|\mathbf{f}_*|)\mathbf{f}_*$ and $|\mathbf{r} \cdot \mathbf{f}_*| + \Phi_1 = 2|\mathbf{r}||\mathbf{f}_*|$. Thus, substituting into (20) yields $\mathbf{f}(\mathbf{r}, \mathbf{g}, \mathbf{h}) = \mathbf{f}_*$, which confirms the result for (ii) $\mathbf{r} \times \mathbf{f}_* = \mathbf{0}$. \square

8. Experiment Setup

This section describes a one-dimensional (1D) experimental platform for testing the EMFF algorithm from Sections 6 and 7, specializes the algorithm to 1D, and presents modifications for implementation.



Figure 3: Experimental platform. Three EAS units sit on the linear air tracks, where the air is supplied by the air sources to create low-friction motion.

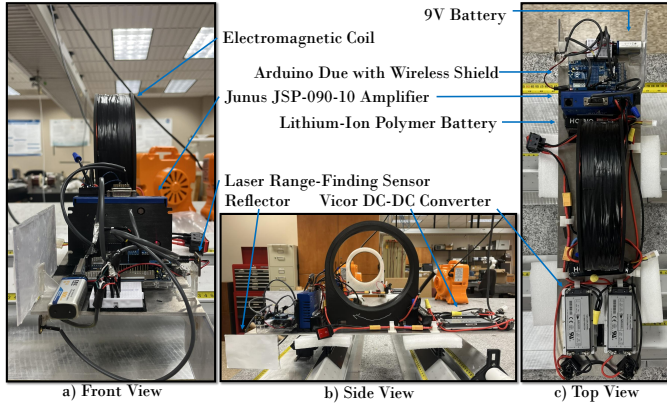


Figure 4: Front view, side view, and top view of the EAS unit on the air track, displaying the power electronics, the arduino, and the laser range-finding sensor.

8.1. Testbed Hardware

The experimental platform is shown in Fig. 3. The testbed includes four Cylone Pro air blowers, two Eisco PH0362A Linear Air Tracks, and three custom-designed one-dimensional electromagnetic actuation system (EAS) units. Each air track is attached to one Cylone Pro air blower. The air blowers supply the required air pressure to the linear air tracks. The EAS units sit on four air track gliders to allow for low friction motion of the units on the

air track. The air tracks are mounted on an aluminum jig-plate which is mounted on a flat and level surface table.

Each EAS unit has an electromagnetic coil and an electrical and electronics platform. Each electromagnetic coil has an area of $A = 0.1\pi^2 \text{ m}^2$ and consists of $N = 500$ turns of 22 gauge copper wire. The impedance of each coil is 71 mH and the resistance is 16 Ohms. The electrical and electronics platforms include all components needed to supply power to the electromagnetic coils. The power electronics consist of two lithium-ion polymer batteries, two Vicor DC-DC converters, and a Copley Controls Junus JSP-090-10 amplifier, as shown in Figure 4. Bench tests were performed to confirm that the amplifiers can produce sinusoidal current commands with the frequency content used in the experiments (i.e., 10 Hz and 20 Hz).

Each EAS unit has an Arduino Due microcontroller which is responsible for data acquisition and feedback control. An XBee radio frequency (RF) module is connected to an Arduino wireless secure digital (SD) shield, which is attached to the microcontroller. A coordinator XBee RF module is also connected to a computer, enabling communication between the computer and the EAS units through a Digi XCTU application. The baud rate of the XBees are set at 115,200, and the data transmission frequency is 2.4 GHz. The satellites' Arduinos start the experiment simultaneously using a transmission from the XBee coordinator. The control is updated with period T to limit frequency drift between the satellites. Although there was no significant time or frequency drift in the experiments, this could be a concern for long-duration maneuvers, necessitating periodic resynchronization of the satellites or adaptive frequency tuning.

The outer EAS units have a single laser ranging module (STM VL53L0X) connected to the microcontroller, while the middle EAS unit has 2 laser-ranging modules on either side. The laser ranging modules are used to measure the unit's position relative to the other unit. The laser ranging module is mounted on an aluminum plate, which forms the base of each EAS unit. The laser ranging module faces a white reflector that is mounted to the other EAS unit.

8.2. Control in 1D with Current Implementation

This section specializes to 1D, where all motion is in the \mathbf{i} direction. Specifically, let $r_{ij,k} \in \mathbb{R}$, $v_{ij,k} \in \mathbb{R}$, and $d_{ij} \in \mathbb{R}$ be such that

$$\mathbf{r}_{ij,k} = r_{ij,k}\mathbf{i}, \quad \mathbf{v}_{ij,k} = v_{ij,k}\mathbf{i}, \quad \mathbf{d}_{ij} = d_{ij}\mathbf{i}, \quad (21)$$

and it follows from (8) that

$$\mathbf{f}_{ij,k}^* = f_{ij,k}^*\mathbf{i}, \quad (22)$$

where the desired value for the intersatellite force function in the \mathbf{i} direction is

$$f_{ij,k}^* \triangleq -\frac{2m|r_{ij,k}|^4}{c_0}\alpha_{ij}((r_{ij,k} - d_{ij}) + \beta v_{ij,k}). \quad (23)$$

For implementation, we do not control magnetic moment (4) directly. Instead, the input is the current $I_i : [0, \infty) \rightarrow \mathbb{R}$ in the i th coil, which is

$$I_i(t) = \sum_{j \in \mathcal{N}_i} I_{ij,k} \sin \omega_{ij} t, \quad (24)$$

where the current amplitudes are

$$I_{ij,k} \triangleq I^*(r_{ij,k}, f_{ij,k}^*, i-j), \quad (25)$$

and

$$I^*(r_{ij,k}, f_{ij,k}^*, i-j) \triangleq \begin{cases} -\frac{\text{sgn}(f_{ij,k}^*)}{NA} \sqrt{\frac{|f_{ij,k}^*|}{2}}, & i-j < 0, \\ \frac{\text{sgn}(r_{ij,k})}{NA} \sqrt{\frac{|f_{ij,k}^*|}{2}}, & i-j > 0. \end{cases} \quad (26)$$

The current control (24) generates a piecewise sinusoidal magnetic moment with frequency ω_{ij} and amplitude

$$p_{ij,k} = NA I_{ij,k}. \quad (27)$$

Thus, (24) generates the magnetic moment (4), where $\mathbf{p}_{ij,k} = p_{ij,k} \mathbf{i}$, which is equal to (18) where $\mathbf{f}_{ij,k}^* = f_{ij,k}^* \mathbf{i}$ and $\mathbf{r}_{ij,k} = r_{ij,k} \mathbf{i}$.

To verify that $\mathbf{f}(r_{ij,k}, \mathbf{p}_{ij,k}, \mathbf{p}_{ji,k}) = \mathbf{f}_{ij,k}^*$, note that since $\mathbf{r}_{ij,k} = r_{ij,k} \mathbf{i}$, and $\mathbf{p}_{ij,k} = p_{ij,k} \mathbf{i}$, it follows from (2) that

$$\mathbf{f}(r_{ij,k}, \mathbf{p}_{ij,k}, \mathbf{p}_{ji,k}) = f(r_{ij,k}, p_{ij,k}, p_{ji,k}) \mathbf{i}, \quad (28)$$

where

$$f(r_{ij,k}, p_{ij,k}, p_{ji,k}) \triangleq -2 \text{sgn}(r_{ij,k}) p_{ij,k} p_{ji,k}. \quad (29)$$

Substituting (25)–(27) into (29) yields $f(r_{ij,k}, p_{ij,k}, p_{ji,k}) = f_{ij,k}^*$, which combined with (22) and (28) demonstrates that $\mathbf{f}(r_{ij,k}, \mathbf{p}_{ij,k}, \mathbf{p}_{ji,k}) = \mathbf{f}_{ij,k}^*$.

8.3. Control Modification to Address Hardware Limitations

We introduce 2 modifications to the current control (23)–(26). First, we introduce integral action to the desired force (23) to address steady-state error. Second, we introduce modifications to the current allocation (25) to address current amplitude saturation. This section redefines $f_{ij,k}^*$ and $I_{ij,k}$ given by (23) and (25) based on these modifications.

Let $\epsilon_0 > 0$ and $\epsilon_1 > \epsilon_0$, and let the integrator state $\xi_{ij,k}$ satisfy

$$\xi_{ij,k} \triangleq \begin{cases} \xi_{ij,k-1} + r_{ij,k} - d_{ij}, & |r_{ij,k} - d_{ij}| \in (\epsilon_0, \epsilon_1), \\ 0, & |r_{ij,k} - d_{ij}| \notin (\epsilon_0, \epsilon_1), \end{cases} \quad (30)$$

where $\xi_{ij,0} \in \mathbb{R}$ is the initial condition. Note that (30) is an integrator if the formation error $r_{ij,k} - d_{ij}$ has small magnitude (i.e., in the interval (ϵ_0, ϵ_1)). Otherwise, the integrator is disabled to prevent integrator windup during the transient phase when the position error can be relatively

large. Then, define the modified desired formation force

$$f_{ij,k}^* \triangleq -\frac{2m|r_{ij,k}|^4}{c_0} (\alpha_{ij}((r_{ij,k} - d_{ij}) + \beta v_{ij,k}) + \rho_{ij} \xi_{ij,k}). \quad (31)$$

where $\rho_{ij} = \rho_{ji} \geq 0$.

Since the intersatellite force depends on the product of $I^*(r_{ij,k}, f_{ij,k}^*, i-j)$ and $I^*(r_{ji,k}, f_{ji,k}^*, j-i)$, equal force can be achieved if one amplitude is increased and the other is decreased proportionally. Thus, we allocate more control authority to satellites with fewer neighbors. To do so, we multiply $I^*(r_{ij,k}, f_{ij,k}^*, i-j)$ with γ_{ij} where $\gamma_{ij} > 0$ and $\gamma_{ji} = 1/\gamma_{ij}$.

Next, define

$$\bar{I}_{i,k} \triangleq \max_{t \in [kT, kT+T)} \left| \sum_{j \in \mathcal{N}_i} \gamma_{ij} I^*(r_{ij,k}, f_{ij,k}^*, i-j) \sin \omega_{ij} t \right|,$$

which is the maximum amplitude of the sum of sinusoidal currents over $t \in [kT, kT+T)$. Since the current is limited by the power capability of the EAS units, we modify $I_{ij,k}$ such that $\bar{I}_{i,k}$ does not exceed the maximum allowable current $\bar{I} > 0$. The current implemented on the i th coil is (24), where the current amplitude is

$$I_{ij,k} \triangleq \begin{cases} \gamma_{ij} I^*(r_{ij,k}, f_{ij,k}^*, i-j), & \bar{I}_{i,k} \leq \bar{I}, \\ \gamma_{ij} \frac{\bar{I}}{\bar{I}_{i,k}} I^*(r_{ij,k}, f_{ij,k}^*, i-j), & \bar{I}_{i,k} > \bar{I}. \end{cases} \quad (32)$$

Then, it follows from (24) and (32) that

$$\max_{t \in [kT, kT+T)} |I_i(t)| \leq \bar{I}, \quad (33)$$

which implies that the current implemented is limited to the maximum allowable current.

Next, we show that the resultant prescribed force is a scaling of the unconstrained prescribed force $f_{ij,k}^*$. Specifically, substituting (26), (27), and (32) into (29) yields

$$f(r_{ij,k}, p_{ij,k}, p_{ji,k}) = \frac{\bar{I}^2}{(\max\{\bar{I}, \bar{I}_{i,k}\})(\max\{\bar{I}, \bar{I}_{j,k}\})} f_{ij,k}^*.$$

Furthermore, (6) and (7) imply that the approximate time-averaged intersatellite force is $\hat{\mathbf{F}}_{ij,k} = \hat{F}(r_{ij,k}, p_{ij,k}, p_{ji,k}) \mathbf{i}$, where

$$\hat{F}(r_{ij,k}, p_{ij,k}, p_{ji,k}) \triangleq \frac{c_0}{2|r_{ij,k}|^4} f(r_{ij,k}, p_{ij,k}, p_{ji,k}). \quad (34)$$

8.4. Relative Position and Velocity Estimation Using a Kalman Filter

Let $q_{ij,k}$ be the measurement of the relative position at time kT , which is taken on satellite i using the onboard sensor. For each satellite, we design Kalman filters, where each Kalman filter uses $q_{ij,k}$ to obtain the estimates $\hat{r}_{ij,k}$ and $\hat{v}_{ij,k}$ of $r_{ij,k}$ and $v_{ij,k}$ for $j \in \mathcal{N}_i$.

It follows from (5)–(7) that $\hat{r}_{ij,k}$ approximately satisfies sampled-data double integrator dynamics where the input is

$$\nu_{ij,k} \triangleq \frac{1}{m} \left(\sum_{g \in \mathcal{N}_i} \hat{F}(\hat{r}_{ig,k}, p_{ig,k}, p_{gi,k}) - \sum_{h \in \mathcal{N}_j} \hat{F}(\hat{r}_{jh,k}, p_{jh,k}, p_{hj,k}) \right). \quad (35)$$

Since satellite i does not have information of all forces acting on satellite j , we consider only the intersatellite forces applied to satellite j by the common neighbors of satellites i and j . Thus, the estimate of $\nu_{ij,k}$ computed onboard satellite i is

$$\hat{\nu}_{ij,k} \triangleq \frac{1}{m} \left(\sum_{g \in \mathcal{N}_i} \hat{F}(\hat{r}_{ig,k}, p_{ig,k}, p_{gi,k}) - \sum_{h \in \{i\} \cup (\mathcal{N}_i \cap \mathcal{N}_j)} \hat{F}(\hat{r}_{jh,k}, p_{jh,k}, p_{hj,k}) \right). \quad (36)$$

Let $V > 0$ be the variance of the noise associated with the measurement $q_{ij,k}$. Then for all k , the filtered relative position $\hat{r}_{ij,k}$ and relative velocity $\hat{v}_{ij,k}$ are given by

$$\begin{bmatrix} \hat{r}_{ij,k} \\ \hat{v}_{ij,k} \end{bmatrix} = (A - LCA) \begin{bmatrix} \hat{r}_{ij,k-1} \\ \hat{v}_{ij,k-1} \end{bmatrix} + (B - LCB) \hat{v}_{ij,k-1} + Lq_{ij,k}, \quad (37)$$

where

$$A \triangleq \begin{bmatrix} 1 & T \\ 0 & 1 \end{bmatrix}, \quad B \triangleq \begin{bmatrix} 0.5T^2 \\ T \end{bmatrix}, \quad C \triangleq [1 \quad 0], \quad (38)$$

and

$$L \triangleq PC^T(CPC^T + V)^{-1}, \quad (39)$$

where P is the solution to the discrete algebraic Riccati equation

$$A^T P A - P - A^T P C (C^T P C + V)^{-1} C^T P A + W = 0, \quad (40)$$

where $W \triangleq w B B^T$ and $w > 0$ is the variance of the disturbance force. The performance of this filter may degrade in the presence of non-Gaussian disturbances (e.g., disturbances from the airflow leaving the airtracks in the experiments, atmospheric drag in low Earth orbit for on-orbit deployment). In this case, other state estimation methods (e.g., particle filters) could be considered.

9. Experimental Results and Discussion

We present results from open-loop and closed-loop experiments using the EAS units described in Section 8 with the control algorithm presented in Section 8.2 with the modifications presented in Section 8.3. The control update period $T = 0.1$ s is selected based on a tradeoff between the computational capability of the microprocessor and

the speed of the closed-loop response. Recall that the approximate time-averaged formation dynamics (i.e., (5) with $\bar{\mathbf{F}}_{ij}(k) = \hat{\mathbf{F}}_{ij,k}$ is developed under the assumption that \mathbf{r}_{ij} does not change significantly over period T . Thus, T is selected to be small enough that this assumption is reasonable and large enough such that all computations can be performed in real time onboard the microprocessor. The plots of the experiments include $|q_{ij,k}|$, $|\hat{r}_{ij,k}|$, $\hat{v}_{ij,k}$, $I_{ij,k}$, and $\hat{F}(r_{ij,k}, p_{ij,k}, p_{ji,k})$. The Kalman filter is initialized with $\hat{r}_{ij,0} = q_{ij,0}$ and $\hat{v}_{ij,0} = 0$ m/s.

9.1. Two-Satellite Validation in Open and Closed Loop

We present 2 open-loop experiments and 3 closed-loop experiments with 2 satellites. The left satellite is numbered 1 and the right satellite is numbered 2. The actuation frequency are $\omega_{12} = \omega_{21} = 40\pi$ rad/s. Using experimental data, we estimate the variances $V = 1.2 \times 10^{-6}$ m² and $w = 5 \times 10^{-6}$ m²/s⁴. It follows from (38)–(40) that

$$P = \begin{bmatrix} 0.2686 & 0.2710 \\ 0.2710 & 0.5206 \end{bmatrix} \times 10^{-6}, \quad L = \begin{bmatrix} 0.2013 \\ 0.1845 \end{bmatrix}.$$

First, we present open-loop experiments to demonstrate that the experimental testbed is capable of generating attractive and repulsive forces.

Experiment 1. This experiment demonstrates open-loop attraction. Figure 5 shows the experimental results, where the first row shows the raw relative-position measurements $|q_{ij}|$, the second and third rows show the filtered measurements $|\hat{r}_{ij}|$ and \hat{v}_{ij} , the fourth row shows the current I_{ij} , and the fifth row shows the time-averaged intersatellite force $\hat{F}(r_{ij,k}, p_{ij,k}, p_{ji,k})$. The first column shows the data measured and computed onboard satellite 1, and the second column shows the data measured and computed onboard satellite 2.

The control is turned on at $t = 5$ s with amplitudes $I_{12} = 1$ A and $I_{21} = 1$ A (sinusoidal currents are in phase). Then, $|\hat{r}_{ij}|$ decreases from 0.508 m to 0.38 m over the next 15 s, which demonstrates attraction. There is a slight offset between the initial estimates $|\hat{r}_{12,0}|$ and $|\hat{r}_{21,0}|$, which resolves at smaller distance. This can be explained by sensor and reflector misalignment, and laser-ranging sensor bias at larger distances. \triangle

Experiment 2. This experiment demonstrates open-loop repulsion. Figure 6 shows that the control is turned on at $t = 5$ s with amplitudes $I_{12} = -1$ A and $I_{21} = 1$ A (sinusoidal currents are out of phase). Then, $|\hat{r}_{ij}|$ increases from 0.404 m to 0.56 m over the next 15 s, which demonstrates repulsion. \triangle

Next, we present 3 experiments demonstrating closed-loop control. The control $(I_{12,k}, I_{21,k})$ is implemented with $\alpha_{ij} = 0.0158$, $\beta = 6.89$, $\rho_{ij} = 0$, and $\bar{I} = 2.35$ A. Note that α_{ij} and β are selected such that $\alpha_{ij} m / (c_0 N^2 A^2) = 812$ and $\alpha_{ij} \beta m / (c_0 N^2 A^2) = 5600$. These gains are selected

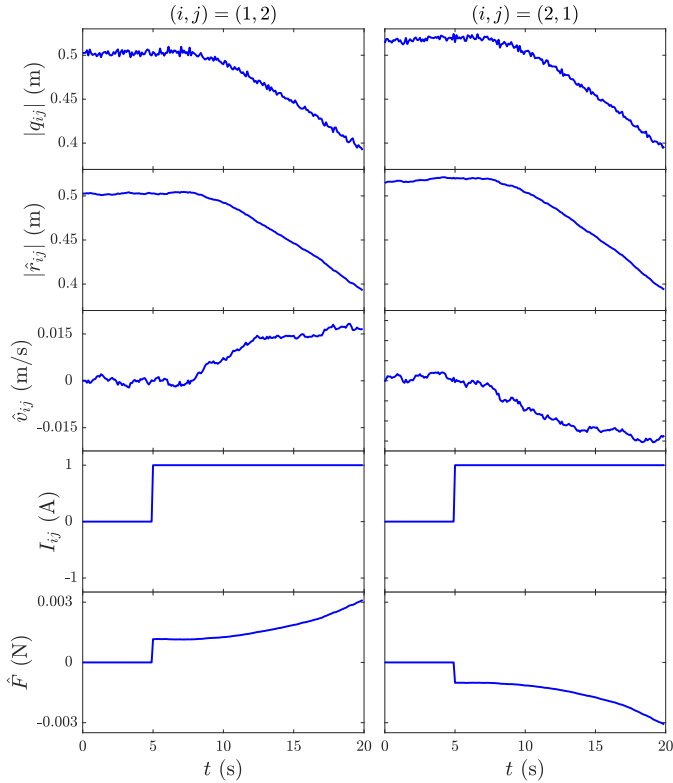


Figure 5: Open-loop attraction between two satellites where $I_{12,k} = 1$ A and $I_{21,k} = 1$ A for $t > 5$ seconds. The sinusoidal currents on the satellites are in phase, which results in an attractive force.

based on a tradeoff between response speed and hardware capability (e.g., current limits). The selected values are such that the settling time and overshoot for the idealized closed-loop double-integrator dynamics are approximately 20 s and less than 0.01 m, respectively.

Experiment 3. This experiment demonstrates closed-loop repulsion. The satellites start at a relative distance of approximately 0.4 m. The objective is to reach a desired relative distance $|d_{ij}| = 0.45$ m. Figure 7 shows that $|\hat{r}_{ij}|$ settles to $|d_{ij}| = 0.45$ m after approximately 20 s. Specifically, the settling time is 21.1 s, and the mean steady-state error $\hat{r}_{ij} - d_{ij}$ over the last 60 s is 2.7×10^{-3} m. Note that there is a sharp decrease in the measurement $|q_{12}|$ at $t = 2.5$ s, which is due to a sensor dropout. The variance of the unfiltered steady-state error $q_{ij} - d_{ij}$ is 3.1×10^{-6} m², where 1.2×10^{-6} m² is attributed to sensor noise and the remaining is potentially due in part to unmodeled external disturbances.

Next, we compare the experimental results with simulations of the closed-loop (3) and (4) where $\mathbf{p}_{ij,k} = p_{ij,k}\mathbf{i}$. We initialize the simulation using the same initial conditions as in the experiment. The simulated relative position includes zero-mean Gaussian-white sensor noise with variance $V = 1.2 \times 10^{-6}$ m², which is the sensor noise variance estimated from experimental data. Then, the filtered relative position and velocity are obtained from the Kalman filter in Section 8.4, which is the method used in the experiment.

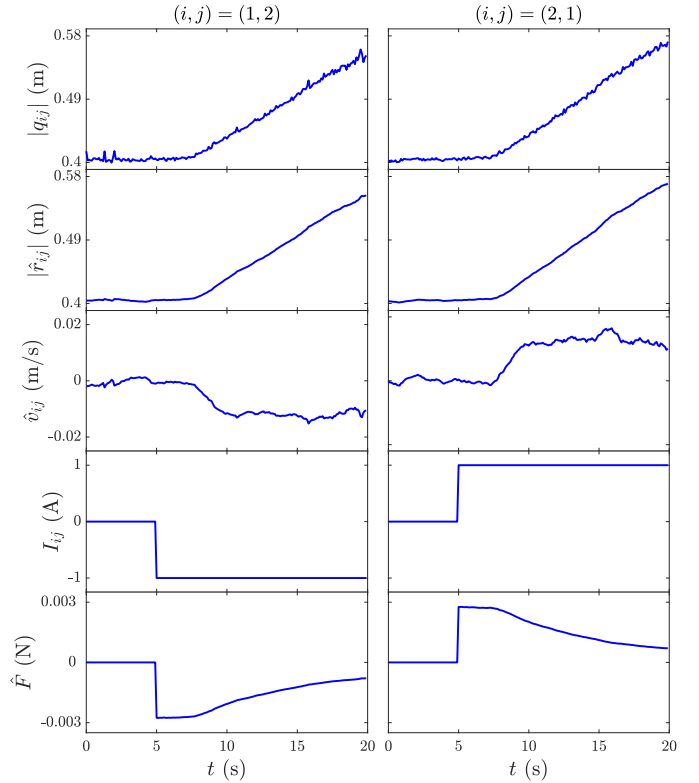


Figure 6: Open-loop repulsion between two satellites where $I_{12,k} = -1$ A and $I_{21,k} = 1$ A for $t > 5$ seconds. The sinusoidal currents on the satellites are out of phase, which results in a repulsive force.

Figure 8 shows the simulation results, which qualitatively match the experimental results in Figure 7.

To compare the experiment and simulation quantitatively, we use 4 metrics: overshoot \hat{r}_{os} ; settling time T_s (i.e. the time it takes \hat{r}_{ij} to reach and stay within 1% of its final value); maximum value of $|\hat{F}(r_{ij,k}, p_{ij,k}, p_{ji,k})|$; and

$$P_{\hat{F}} \triangleq \sqrt{\frac{1}{N_t} \sum_{k=1}^{N_t} \hat{F}(r_{ij,k}, p_{ij,k}, p_{ji,k})^2}, \quad (41)$$

which is the root mean square of the force, where N_t is the number of data points. Table 1 presents these metrics for the experiment and the simulation. The experiment and the simulation have similar T_s and $\max|\hat{F}|$. The difference in these metrics between the experiment and simulation is less than 15%. The experiment has 70% more overshoot than the simulation; however, the overshoot is small (less than 1 cm) for both. The root mean square of the force in the experiment is 51% larger than in the simulation. These differences can be partly explained by external disturbances present in the experiment that are not included in the simulation. For example, the airtracks are not perfectly level over the entire length; the airflow from the airtracks creates disturbances forces; and the initial velocity in the experiment is not perfectly known, so there is mismatch between this condition in the experiment and

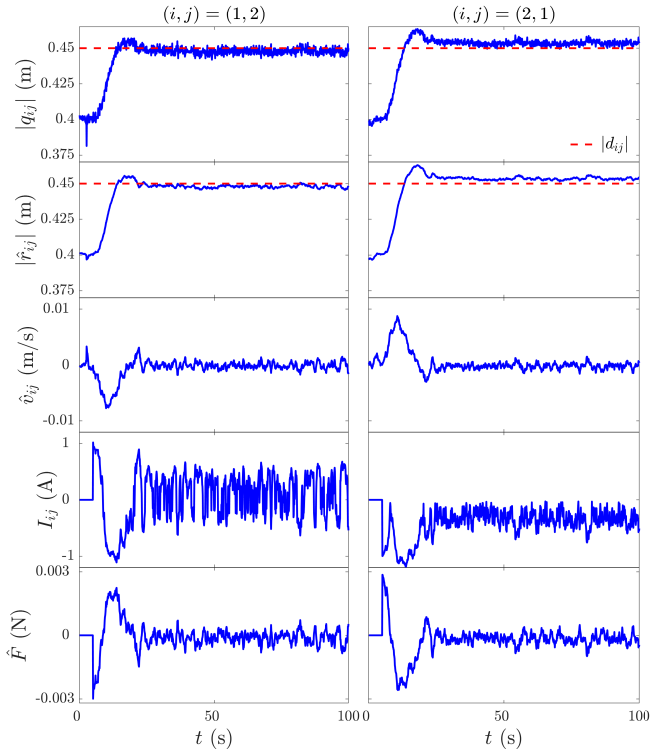


Figure 7: Experiment demonstrating closed-loop repulsion with 2 satellites, where the satellites start at approximately 0.4 m apart, and the desired relative position is $|d_{ij}| = 0.45$ m.

the simulation. Differences can also be partly explained by near-field electromagnetic effects [24] that are not included in the simulation. \triangle

Table 1: Metrics for Experiment 3 and Simulation

	Experiment 3		Simulation	
	$(i, j) = (1, 2)$	$(i, j) = (2, 1)$	$(i, j) = (1, 2)$	$(i, j) = (2, 1)$
\hat{r}_{os} (cm)	0.76	0.95	0.55	0.47
T_s (s)	21.0	21.1	18.3	18.3
$\max \hat{F} $ (N)	2.99×10^{-3}	2.85×10^{-3}	2.67×10^{-3}	2.61×10^{-3}
$P_{\hat{F}}$ (N)	2.02×10^{-4}	2.27×10^{-4}	1.43×10^{-4}	1.41×10^{-4}

Experiment 4. This experiment demonstrates closed-loop attraction. The satellites start at a relative distance of approximately 0.5 m. The objective is to reach a desired relative distance $|d_{ij}| = 0.45$ m. Figure 9 shows that $|\hat{r}_{ij}|$ settles to $|d_{ij}| = 0.45$ m after approximately 20 s. Specifically, the settling time is 21.0 s, and the mean steady-state error $\hat{r}_{ij} - d_{ij}$ over the last 60 s is 3.8×10^{-3} m. Note that the satellites move before the control is turned on at $t = 5$ s. This can be explained by a slight impulse introduced at the start of the experiment and airflow from the airtracks creating disturbances. The variance of the unfiltered steady-state error $q_{ij} - d_{ij}$ is 3.3×10^{-6} m², which is comparable to Experiment 3.

Figure 10 shows the simulation results, which qualitatively matches the experimental results in Figure 9. Table 2

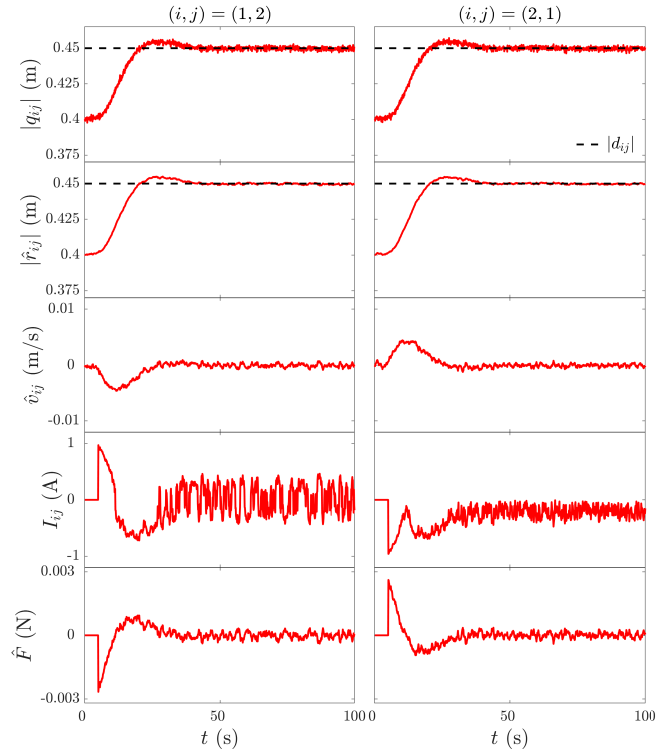


Figure 8: Simulation of closed-loop repulsion with 2 satellites, where the satellites start at approximately 0.4 m apart, and the desired relative position is $|d_{ij}| = 0.45$ m.

presents the metrics \hat{r}_{os} , T_s , $\max|\hat{F}|$, and $P_{\hat{F}}$. The quantitative comparison is similar to Experiment 3. In particular, T_s and $\max|\hat{F}|$ are comparable between the experiment and the simulation. The difference in these metrics between the experiment and simulation is less than 15%. In contrast, \hat{r}_{os} and $P_{\hat{F}}$ are larger in the experiment. These differences can be attributed to the causes discussed in Experiment 3. \triangle

Table 2: Metrics for Experiment 4 and Simulation

	Experiment 4		Simulation	
	$(i, j) = (1, 2)$	$(i, j) = (2, 1)$	$(i, j) = (1, 2)$	$(i, j) = (2, 1)$
\hat{r}_{os} (cm)	1.02	1.22	0.59	0.58
T_s (s)	20.9	21.0	18.8	18.7
$\max \hat{F} $ (N)	2.79×10^{-3}	3.38×10^{-3}	3.48×10^{-3}	3.22×10^{-3}
$P_{\hat{F}}$ (N)	2.38×10^{-4}	2.62×10^{-4}	1.66×10^{-4}	1.64×10^{-4}

Experiment 5. This experiment demonstrates multiple maneuvers in succession. The satellites start at a relative distance of approximately 0.50 m. The initial objective is to reach a desired relative distance $|d_{ij}| = 0.4$ m. Next, the desired relative position is switched to 0.5 m at $t = 60$ s. Figure 11 shows that $|\hat{r}_{ij}|$ settles to $|d_{ij}| = 0.40$ m at approximately 35 s, and $|\hat{r}_{ij}|$ settles to $|d_{ij}| = 0.50$ m by approximately 90 s, which demonstrates that the satellites can achieve multiple formation maneuvers. The current

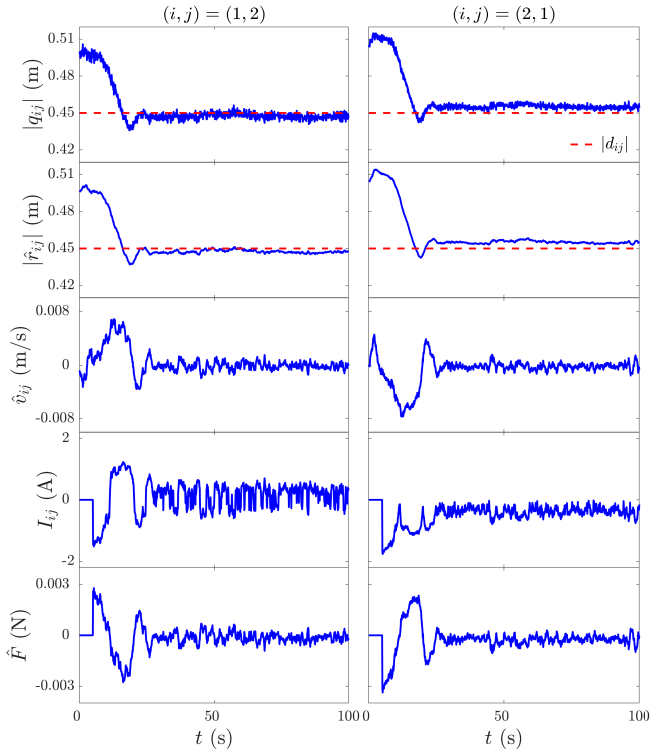


Figure 9: Experiment demonstrating closed-loop attraction with 2 satellites, where the satellites start at approximately 0.5 m apart, and the desired relative position is $|d_{ij}| = 0.45$ m.

amplitude saturation (32) is active from 5.1 s to 6.3 s. During this time interval, the unsaturated current amplitudes exceed the limit $\bar{I} = 2.35$ A. The peak unsaturated amplitude is 2.77 A, which occurs at 5.3 s and corresponds to a desired force of 0.0078 N. Since the amplitude is saturated, the time-averaged force is only 0.0062 N, which is 20% less than the desired value. This demonstrates that the control approach has some robustness to the current amplitude limits imposed by the hardware. Figure 12 shows the simulation results, which qualitatively matches the experimental results in Figure 11. \triangle

9.2. Three-Satellite Closed-Loop Formation Experiments

Next, we present 3 closed-loop experiments with $n = 3$ satellites. The middle, left, and right satellites are numbered 1, 2, and 3. The neighbor sets are $\mathcal{N}_1 = \{2, 3\}$, $\mathcal{N}_2 = \{1\}$, and $\mathcal{N}_3 = \{1\}$. The interaction frequencies are selected as the 2 smallest common multiples of $2\pi/T$, where $T = 0.1$ s. Specifically, $\omega_{12} = \omega_{21} = 20\pi$ rad/s and $\omega_{13} = \omega_{31} = 40\pi$ rad/s. The smallest common multiples are used because lower frequency results in smaller impedance and larger maximum allowable current. We implement the currents $(I_{ij,k}, I_{ji,k})$ given by (31)–(32) with $\epsilon_0 = 0.015$ m, $\epsilon_1 = 0.021$ m, $\alpha_{ij} = 0.0158$, $\beta = 7.38$, $\rho_{ij} = 0.00136$, $\gamma_{12} = \gamma_{13} = 0.8$ and $\gamma_{21} = \gamma_{31} = 1.25$, and $\bar{I} = 2.35$ A. Note that we select α_{ij} , β , and ρ_{ij} such that $\alpha_{ij}m/(c_0N^2A^2) = 812$, $\alpha_{ij}\beta m/(c_0N^2A^2) = 6000$, and $\rho_{ij}m/(c_0N^2A^2) = 70$. The gains α_{ij} , β , and ρ_{ij} are se-

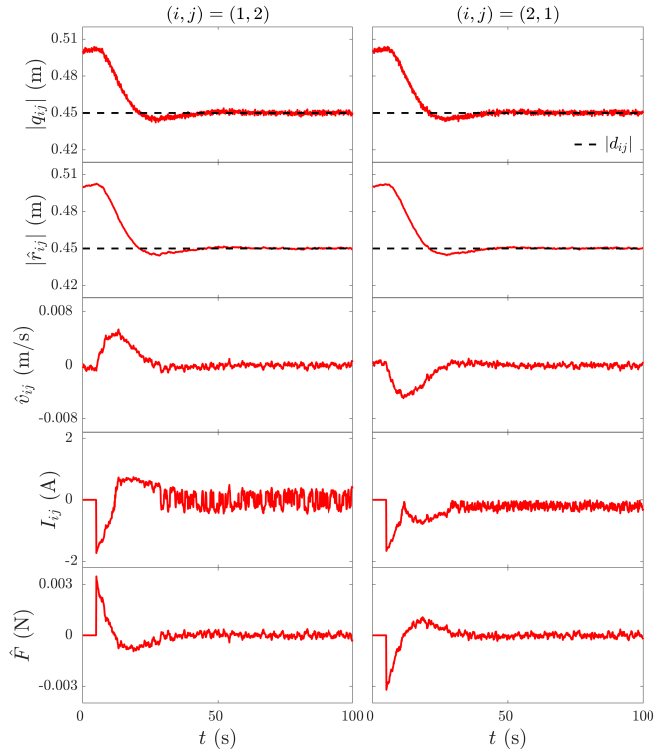


Figure 10: Simulation of closed-loop attraction with 2 satellites, where the satellites start at approximately 0.5 m apart, and the desired relative position is $|d_{ij}| = 0.45$ m.

lected based on simulation responses. Using experimental data, we estimate the variances $V = 2 \times 10^{-6}$ m² and $w = 5 \times 10^{-6}$ m²/s⁴. It follows from (38)–(40) that

$$P = \begin{bmatrix} 0.3891 & 0.3456 \\ 0.3456 & 0.5879 \end{bmatrix} \times 10^{-6}, \quad L = \begin{bmatrix} 0.1773 \\ 0.1447 \end{bmatrix}.$$

Experiment 6. This experiment demonstrates closed-loop repulsion between satellites 1 and 2, and closed-loop repulsion between satellites 1 and 3. Satellites 1 and 2 start at a relative distance of approximately 0.35 m, and satellites 1 and 3 start at a relative distance of approximately 0.38 m apart. The objective is to reach the desired relative positions $d_{12} = 0.42$ m and $d_{13} = -0.45$ m. Figure 13 shows the experimental results, where the column on the left shows relative measurements, estimates, and time-averaged approximate force between satellite 2 (left satellite) and satellite 1 (middle satellite), as measured and computed on satellite 2; and the second column from the left shows the data as measured and computed on satellite 1. The third column from the left shows relative measurements, estimates, and time-averaged approximate force between satellite 1 and satellite 3 (right satellite), as measured and computed on satellite 1; and the column on the right shows the data as measured and computed on satellite 3. Figure 13 shows that \hat{r}_{12} and \hat{r}_{13} converges to d_{12} and d_{13} after approximately 26 s. For satellites 1 and 2, the settling time is 28.3 s, and the mean steady-state

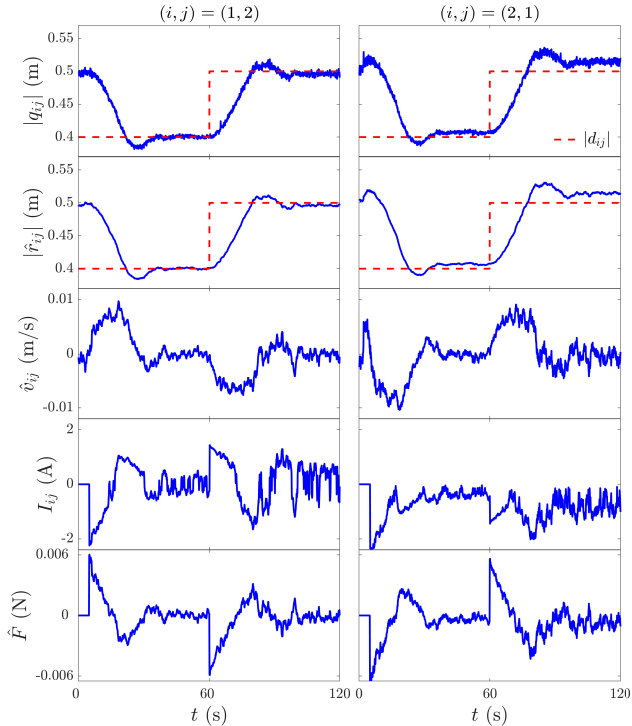


Figure 11: Experiment demonstrating multiple maneuvers with 2 satellites, where the satellites start at approximately 0.5 m apart. The initial desired relative position is $|d_{ij}| = 0.4$ m, and at 60 s the desired relative position is switched to $|d_{ij}| = 0.5$ m.

error $\hat{r}_{12} - d_{12}$ over the last 60 s is 1.0×10^{-3} m. For satellites 1 and 3, the settling time is 26.4 s, and the mean steady-state error $\hat{r}_{13} - d_{13}$ over the last 60 s is 0.9×10^{-3} m. The variance of the unfiltered steady-state error $q_{ij} - d_{ij}$ is 4.1×10^{-6} m², where 2×10^{-6} is attributed to sensor noise variance and the remaining is potentially due in part to unmodeled external disturbances.

Next, we present simulations of the closed-loop (3) and (4) where $\mathbf{p}_{ij,k} = p_{ij,k}\mathbf{i}$. The effect of friction between the satellites and the linear air tracks becomes noticeable with the addition of the third satellite. This effect is modeled by including linear damping $b_i v_i \mathbf{i}$ in (3), where selecting b_i involves a tradeoff between reducing response oscillations and increasing settling time. Larger b_i tends to decrease oscillations but increase settling time. The damping coefficient $b_i = 0.08$ N-s/m is selected to achieve a similar response to the experiments. The simulated relative position includes zero-mean Gaussian-white sensor noise with variance $V = 2 \times 10^{-6}$ m², which is the sensor noise variance estimated from experimental data. Figure 14 shows the simulation results, which qualitatively agree with the experimental results. However, we observe an oscillatory transient response in Figure 14, which is not observed in Figure 13. This can partly be explained by the imperfect friction model, unmodeled external disturbances (e.g., lateral air pressure from the air track), and unmodeled near-field electromagnetic effects. \triangle

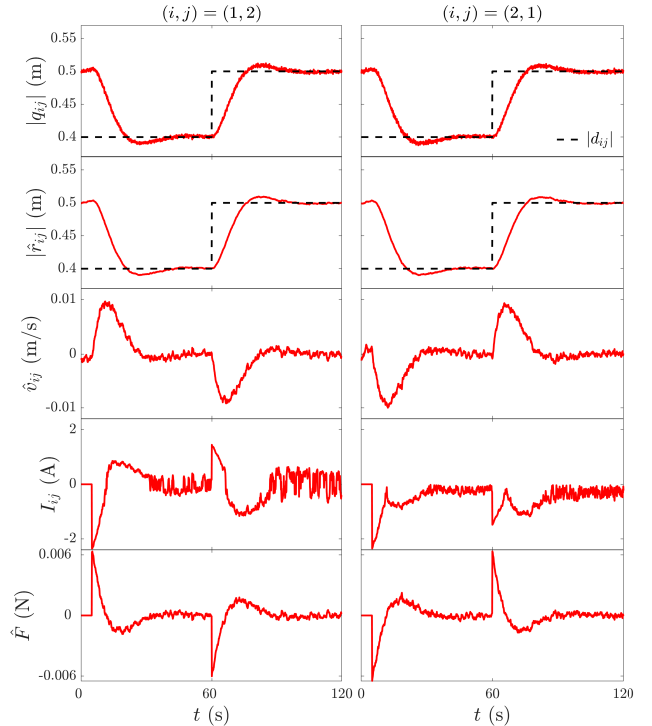


Figure 12: Simulation demonstrating multiple maneuvers with 2 satellites, where the satellites start at approximately 0.5 m apart. The initial desired relative position is $|d_{ij}| = 0.4$ m, and at 60 s the desired relative position is switched to $|d_{ij}| = 0.5$ m.

Experiment 7. This experiment demonstrates closed-loop attraction between satellite 1 and satellite 2, and closed-loop attraction between satellite 1 and satellite 3. Satellites 1 and 2 start at a relative distance of approximately 0.425 m, and satellites 1 and 3 start at a relative distance of approximately 0.46 m. The objective is to reach the desired relative positions $d_{12} = 0.35$ m and $d_{13} = -0.38$ m. Figure 15 shows that \hat{r}_{12} and \hat{r}_{13} converges to the desired relative positions d_{12} and d_{13} by approximately 26 s. For satellites 1 and 2, the settling time is 23.1 s, and the mean steady-state error $\hat{r}_{12} - d_{12}$ over the last 60 s is 0.7×10^{-3} m. For satellites 1 and 3, the settling time is 25.5 s, and the mean steady-state error $\hat{r}_{13} - d_{13}$ over the last 60 s is 0.8×10^{-3} m. The variance of the unfiltered steady-state error $q_{ij} - d_{ij}$ is 4.1×10^{-6} m², which is comparable to Experiment 6. Figure 16 shows the simulation results, which qualitatively agree with the experimental results. Similar to the comparison in Experiment 6, the simulation has oscillatory overshoot whereas the overshoot in the experiment decays more quickly. \triangle

Experiment 8. This experiment demonstrates closed-loop attraction between satellite 1 and satellite 2, and closed-loop repulsion between satellite 1 and satellite 3. Satellites 1 and 2 start at a relative distance of approximately 0.46 m, and satellites 1 and 3 start at a relative distance of approximately 0.38 m apart. The objective is to reach the desired relative positions $d_{12} = 0.42$ m and $d_{13} = -0.45$ m. Figure 17 shows that \hat{r}_{12} and \hat{r}_{13}

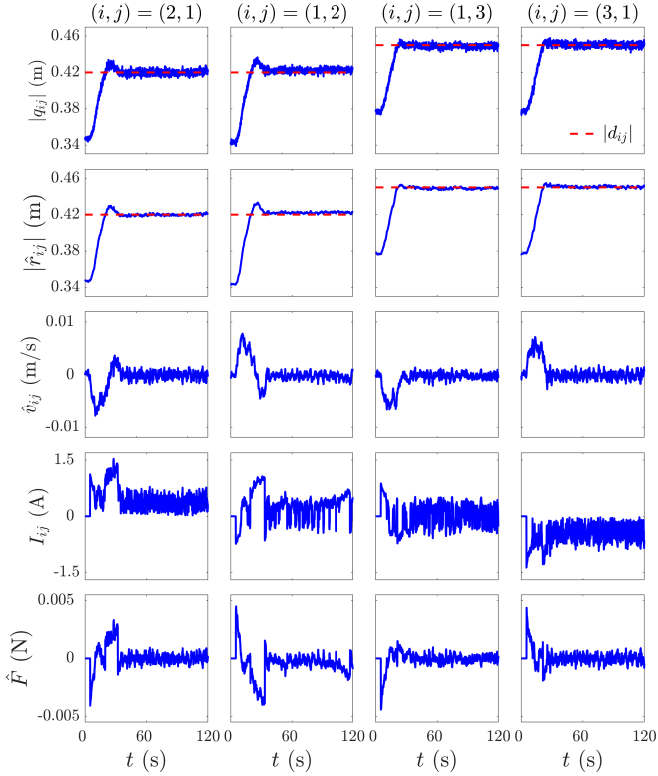


Figure 13: Experiment demonstrating closed-loop repulsion between satellite 1 and 2 and closed-loop repulsion between satellite 1 and 3. Initially, satellites 1 and 2 are approximately 0.346 m apart, and satellites 1 and 3 are approximately 0.377 m apart. The desired relative positions are $d_{12} = 0.42$ m, and $d_{13} = -0.45$ m.

converges to the desired relative position d_{12} and d_{13} by approximately 25 s. For satellites 1 and 2, the settling time is 24.6 s, and the mean steady-state error $\hat{r}_{12} - d_{12}$ over the last 60 s is 1.2×10^{-3} m. For satellites 1 and 3, the settling time is 24.4 s, and the mean steady-state error $\hat{r}_{13} - d_{13}$ over the last 60 s is 1.6×10^{-3} m. The variance of the unfiltered steady-state error $q_{ij} - d_{ij}$ is 4.0×10^{-6} m², which is comparable to Experiment 6 and Experiment 7. Figure 18 shows the simulation of the experiment, which qualitatively matches the experimental results in Figure 17. \triangle

Table 3 is a summary of experimental results, including the settling time, mean steady-state error $\hat{r}_{ij} - d_{ij}$ over the last 60 s, variance of the steady-state error over last 60 s, and the maximum steady-state error over last 60 s.

Table 3: Settling time, mean steady-state error, variance of steady-state error, and maximum steady-state error

Experiment	T_s (s)	Mean steady-state error (m)	Variance (m ²)	Maximum steady-state error (m)
3	21.1	2.7×10^{-3}	8.1×10^{-7}	6.0×10^{-3}
4	21.0	3.8×10^{-3}	13.7×10^{-7}	8.3×10^{-3}
6	27.3	0.95×10^{-3}	7.4×10^{-7}	4.1×10^{-3}
7	24.3	0.75×10^{-3}	3.9×10^{-7}	4.0×10^{-3}
8	24.5	1.4×10^{-3}	5.2×10^{-7}	5.4×10^{-3}

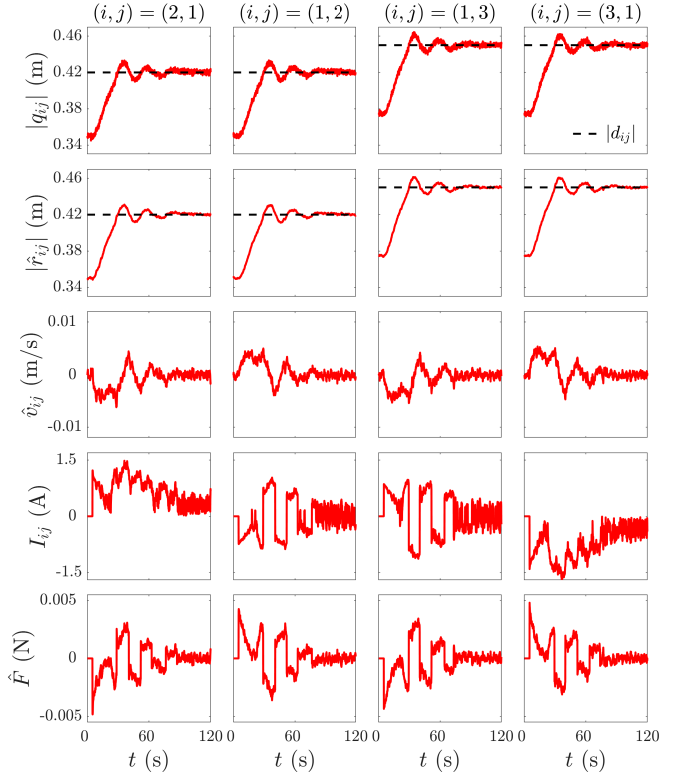


Figure 14: Simulation demonstrating closed-loop repulsion between satellite 1 and 2 and closed-loop repulsion between satellite 1 and 3. Initially, satellites 1 and 2 are approximately 0.346 m apart, and satellites 1 and 3 are approximately 0.377 m apart. The desired relative positions are $d_{12} = 0.42$ m, and $d_{13} = -0.45$ m.

10. Concluding Remarks

This article presented a 3-satellite experimental demonstration of decentralized EMFF using AMFF. To the authors' knowledge, this is the first demonstration of AMFF with at least 3 satellites in open or closed loop. The experimental results not only demonstrate the feasibility of EMFF with AMFF but also demonstrate that the frequency-multiplexed amplitude-modulated sinusoidal approach can be used to achieve formation with multiple satellites. Specifically, the closed-loop experiments demonstrate decentralized EMFF with AMFF for 3 satellites where the mean steady-state formation error is less than 0.005 m, the maximum steady-state formation error is less than ± 0.01 m, and the settling time is less than 30 s. The experiments also show that the approach in this paper provides robustness to hardware limitations (e.g., power limits, sensor noise). However, future experimental studies could adopt the AMFF control methods in [23] to explicitly account for constraints (e.g., power/current limits, thermal management of the coils) using a composite control barrier function.

Future experimental studies could focus on considerations that are relevant for in-space testing and deployment. Although the method in this article applies to 3-degree-of-freedom position control, the experiments are restricted

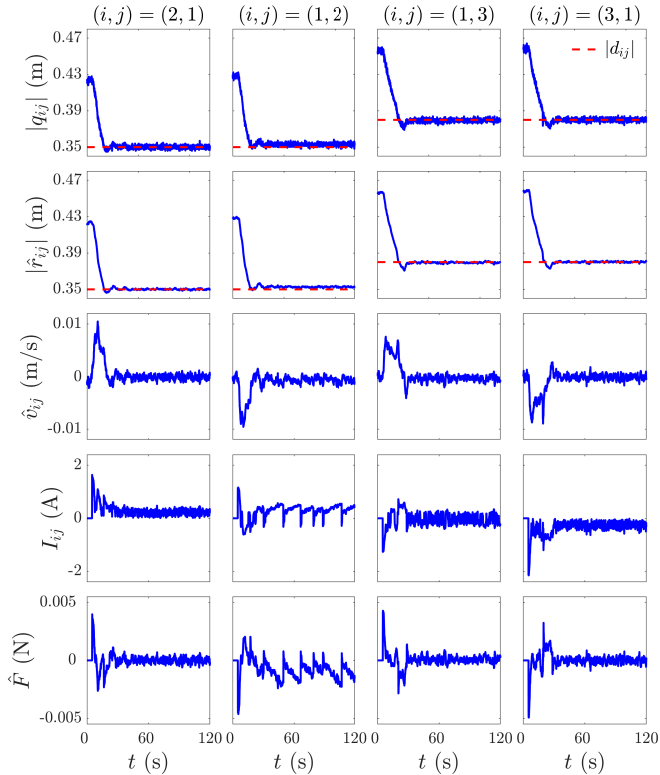


Figure 15: Experiment demonstrating closed-loop attraction between satellite 1 and 2 and closed-loop attraction between satellite 1 and 3. Initially, satellites 1 and 2 are approximately 0.425 m apart, and satellites 1 and 3 are approximately 0.46 m apart. The desired relative positions are $d_{12} = 0.35$ m, and $d_{13} = -0.38$ m.

to a single degree of freedom. Future experiments could include ground-based 3-degree-of-freedom experiments (planar translation and one-degree-of-freedom attitude control). Such experiments would require multiple electromagnetic coils (e.g., 2 orthogonal coils for control in the plane) and additional interaction frequencies for relative attitude control [15]. Similarly, 6-degree-of-freedom would require at least 3 electromagnetic coils. In this case, hardware design is tightly interlinked with power requirements, computational complexity of the control algorithms, and acceptable performance levels.

Other important considerations for on-orbit deployment include accounting for gravitational forces (which is addressed in [23]), disturbances such as atmospheric drag in low Earth orbit, and other space environment effects (e.g., radiation, extreme heat-cold cycles, Earth's magnetic field).

Conflict of Interest Statement

There is no conflict of interest.

Acknowledgments

This work is supported in part by the National Aeronautics and Space Administration (80NSSC17M0040), the

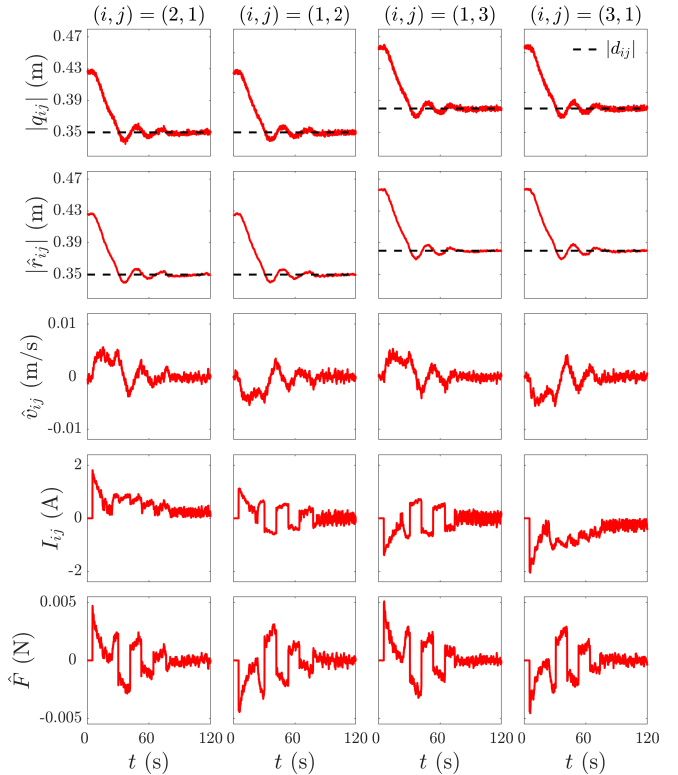


Figure 16: Simulation demonstrating closed-loop attraction between satellite 1 and 2 and closed-loop attraction between satellite 1 and 3. Initially, satellites 1 and 2 are approximately 0.425 m apart, and satellites 1 and 3 are approximately 0.46 m apart. The desired relative positions are $d_{12} = 0.35$ m, and $d_{13} = -0.38$ m.

National Science Foundation (1932105), and the Air Force Office of Scientific Research (FA9550-20-1-0028).

We would like to thank Floyd Taylor, Herb Mefford, and Jonathan T. Williams at the University of Kentucky for their invaluable advice on improving the physical testbed.

References

- [1] E. M. C. Kong, D. W. Kwon, S. A. Schweighart, L. M. Elias, R. J. Sedwick, D. W. Miller, Electromagnetic formation flight for multisatellite arrays, *J. Spacecraft and Rockets* 41 (4) (2004) 659–666.
- [2] D. W. Kwon, Propellantless formation flight applications using electromagnetic satellite formations, *Acta Astronautica* 67 (9) (2010) 1189–1201.
- [3] A. K. Porter, D. J. Alinger, R. J. Sedwick, J. Merk, R. A. Opperman, A. Buck, G. Eslinger, P. Fisher, D. W. Miller, E. Bou, Demonstration of electromagnetic formation flight and wireless power transfer, *J. Spacecraft and Rockets* 51 (6) (2014) 1914–1923.
- [4] L. M. Elias, D. W. Kwon, R. J. Sedwick, D. W. Miller, Electromagnetic formation flight dynamics including reaction wheel gyroscopic stiffening effects, *J. Guid., Contr., Dyn.* 30 (2) (2007) 499–511.

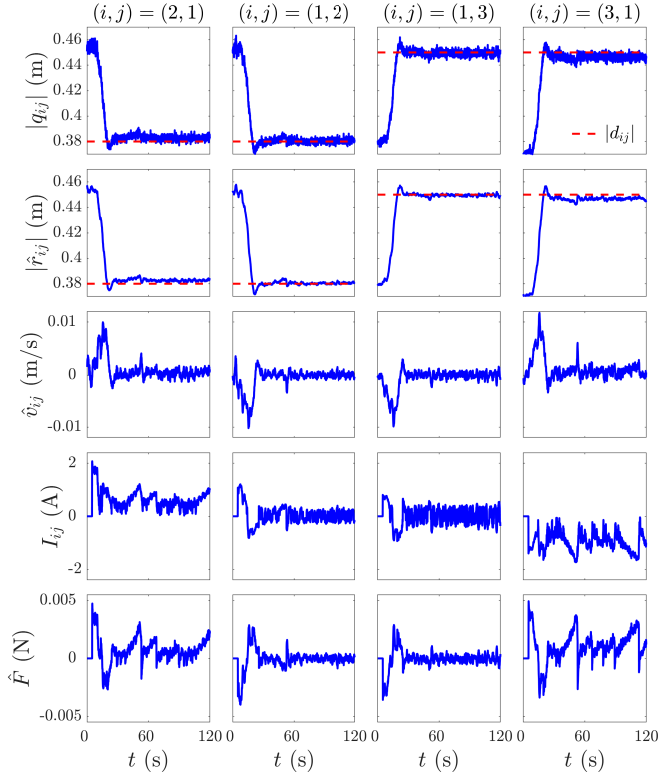


Figure 17: Experiment demonstrating closed-loop attraction between satellite 1 and 2 and closed-loop repulsion between satellite 1 and 3. Initially, satellites 1 and 2 are approximately 0.46 m apart, and satellites 1 and 3 are approximately 0.38 m apart. The desired relative positions are $d_{12} = 0.42\text{m}$ and $d_{13} = -0.45\text{ m}$.

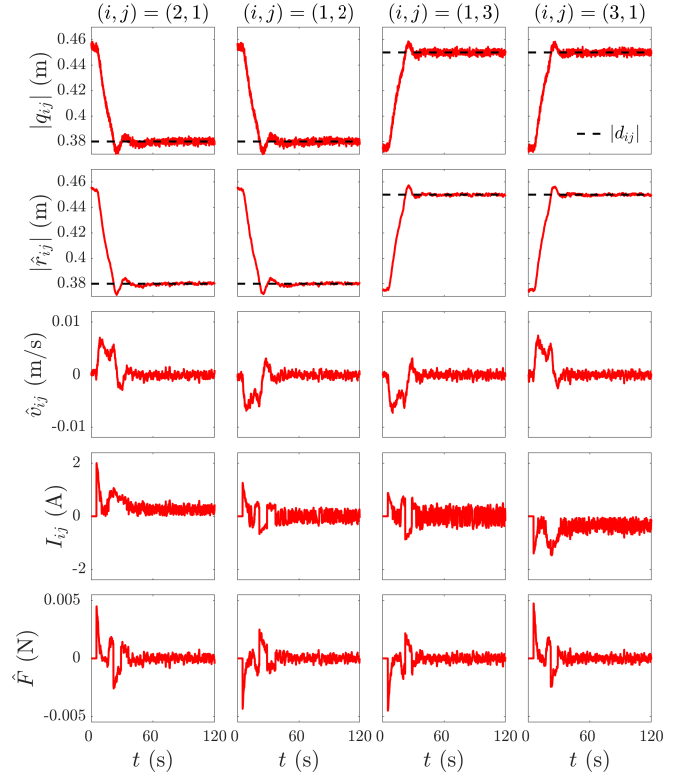


Figure 18: Simulation demonstrating closed-loop attraction between satellite 1 and 2 and closed-loop repulsion between satellite 1 and 3. Initially, satellites 1 and 2 are approximately 0.46 m apart, and satellites 1 and 3 are approximately 0.38 m apart. The desired relative positions are $d_{12} = 0.42\text{m}$ and $d_{13} = -0.45\text{ m}$.

- [5] D. W. Kwon, R. J. Sedwick, S.-i. Lee, J. L. Ramirez-Riberos, Electromagnetic formation flight testbed using superconducting coils, *J. Spacecraft and Rockets* 48 (1) (2011) 124–134.
- [6] U. Ahsun, D. Miller, Dynamics and control of electromagnetic satellite formations, in: *Proc. Amer. Contr. Conf.*, 2006, pp. 1730–1735.
- [7] S. A. Schweighart, R. J. Sedwick, Explicit dipole trajectory solution for electromagnetically controlled spacecraft clusters, *J. Guid., Contr., Dyn.* 33 (4) (2010) 1225–1235.
- [8] Y. Cai, C. Zhang, J. Wu, S. Yang, Spatial static configuration design and formation control of multiple electromagnetic spacecrafts, in: *Chinese Control Conference*, 2023, pp. 593–598.
- [9] J. L. Ramirez Riberos, New decentralized algorithms for spacecraft formation control based on a cyclic approach, Ph.D. thesis, Dept. of Aeronautics and Astronautics, Massachusetts Institute of Technology (2010).
- [10] R. C. Youngquist, M. A. Nurge, S. O. Starr, Alternating magnetic field forces for satellite formation flying, *Acta Astronautica* 84 (2013) 197–205.
- [11] M. A. Nurge, R. C. Youngquist, S. O. Starr, A satellite formation flying approach providing both positioning and tracking, *Acta Astronautica* 122 (2016) 1–9.
- [12] Z. Abbasi, J. B. Hoagg, T. M. Seigler, Decentralized electromagnetic formation flight using alternating magnetic field forces, *IEEE Trans. Contr. Sys. Tech.* 30 (6) (2022) 2480–2489.
- [13] X. Huang, C. Zhang, H. Lu, H. Yin, An lmi-based decoupling control for electromagnetic formation flight, *Chinese Journal of Aeronautics* 28 (2) (2015) 508–517.
- [14] C. Zhang, X.-L. Huang, Angular-momentum management of electromagnetic formation flight using alternating magnetic fields, *Journal of Guidance, Control, and Dynamics* 39 (6) (2016) 1292–1302.
- [15] Z. Abbasi, J. Hoagg, T. M. Seigler, Decentralized position and attitude based formation control for satellite systems with electromagnetic actuation, in: *AIAA Scitech Forum*, no. AIAA 2020-0617, 2020.
- [16] Y. Song, Q. Zhou, Q. Chen, Control of electromagnetic formation flight of two satellites in low earth orbits, *Aerospace* 10 (3) (2023).

- [17] Y. Song, Q. Zhou, Q. Chen, J. Diao, Decoupling control of electromagnetic formation flight in near-earth orbit, in: Chinese Control Conference, 2023, pp. 6129–6134.
- [18] Y. Takahashi, H. Sakamoto, S.-i. Sakai, Kinematics control of electromagnetic formation flight using angular-momentum conservation constraint, *J. Guid., Contr., Dyn.* 45 (2) (2022) 280–295.
- [19] Z. Abbasi, A. Sunny, J. B. Hoagg, T. M. Seigler, Relative-position formation control of satellites using electromagnetic actuation with piecewise-sinusoidal controls, in: 2020 American Control Conference (ACC), 2020, pp. 4951–4956. doi:10.23919/ACC45564.2020.9147724.
- [20] Y. Takahashi, S. Shim, Y. Sawanishi, H. Yoshikado, M. Ishida, N. Imamura, S. Morioka, S.-i. Sakai, T. Inagawa, Experimental study of magnetically-actuated satellite swarm: Controllability extension via time-integrated control with geometry learning, in: Proc. SMC-IT/SCC Space Robotics Workshop, 2025.
- [21] Y. Cao, W. Ren, Multi-vehicle coordination for double-integrator dynamics under fixed undirected/directed interaction in a sampled-data setting, *International Journal of Robust and Nonlinear Control* 20 (9) (2010) 987–1000.
- [22] S. S. Kamat, T. M. Seigler, J. B. Hoagg, Electromagnetic formation flying with state and input constraints using alternating magnetic field forces, in: 2025 American Control Conference (ACC), 2025, pp. 1701–1706.
- [23] S. S. Kamat, T. M. Seigler, J. B. Hoagg, Electromagnetic formation flying using alternating magnetic field forces and control barrier functions for state and input constraints, *IEEE Transactions on Aerospace and Electronic Systems* (2026) 1–17doi:10.1109/TAES.2026.3664815.
- [24] S. A. Schweighart, Electromagnetic formation flight dipole solution planning, Ph.D. thesis, Dept. of Aeronautics and Astronautics, Massachusetts Institute of Technology (2005).